

Compression and Shaping of Femtosecond Laser Pulses for Coherent Two-Dimensional Nanoscopy

Lukas Wittenbecher

Thesis submitted for the degree of Master of Science



LUND
UNIVERSITY

Supervised by
Anders Mikkelsen and Donatas Zigmantas

Department of Physics
Division of Synchrotron Radiation Research

Department of Chemistry
Division of Chemical Physics

May 2016

Abstract

Femtosecond pulse shaping is a versatile tool that enables the generation of ultrashort laser pulses with nearly arbitrary temporal shapes. Among others, the technique is of use in ultrafast spectroscopy experiments where it can be employed for dispersion control and the generation of well-defined laser pulse sequences.

In this work, a Fourier-transform pulse shaper based on a pixelated liquid crystal spatial light modulator (LC-SLM) was implemented and calibrated. The pulse shaper is designed for phase and amplitude shaping of femtosecond laser pulses in the visible and near-infrared spectral range. A distinctive feature of the setup is the use of a prism to spatially separate the spectral components of the input pulses.

For accurate pulse shaping a careful calibration of the setup is required. Procedures for determining the pixel-to-wavelength and the wavelength dependent voltage-to-phase mapping of the LC-SLM were implemented. The phase is retrieved from the measured intensity modulation behaviour of the pulse shaper using an iterative optimisation algorithm. Estimates for the limitations of the pulse shaper were derived from a theoretical analysis of the wavelength calibration results.

To validate the calibration results, the pulse shaper was used to arbitrarily shape the spectral amplitude of near-infrared laser pulses. Within the limitations of the pulse shaper, good agreement between measured and desired spectral shape was found, confirming the validity of the calibration procedure.

To verify the phase shaping capabilities of the pulse shaper, it was used in combination with a prism compressor to compensate for material dispersion introduced by the dispersive prism in the setup. Dispersion compensation could be successfully demonstrated, albeit bandwidth-limited pulse durations were not achieved.

This work provides a platform for pulse-shaper-assisted ultrafast spectroscopy experiments.

Acknowledgements

First and foremost, I would like to thank my main supervisor Donatas. Thank you for your time and knowledge, for introducing me to the world of femtosecond spectroscopy and for your faith in my capabilities.

I would also like to express my gratitude to my co-supervisor Anders for valuable advice and fruitful discussions.

To all the members of the 2D group I had the luck to meet during the last year, Egle, Erling, David, Kil, Marcelo and Paulius, thank you for the good spirit and numerous enjoyable discussions.

Special thanks go to Marcelo for teaching me all the practical skills I needed for this project during countless hours in the lab, for valuable discussions and for always being available when I was in need of help in the lab. Without your help, this project would not have been possible and I very much enjoyed working with you.

Thanks to my office companions Daniel and Khadga for the laughs we had, for making working on my thesis a much more enjoyable experience and for practical lessons in Mexican food culture.

I would also like to thank all the members of chemical physics for the nice work atmosphere at the department and for Friday fikas and football matches.

I would like to thank my parents for their continuous support and encouragement. Veronika, thank you for your support, your patience and for always being there for me.

Contents

1. Introduction	1
1.1. Motivation	1
1.2. Outline	3
2. Background	4
2.1. Properties of femtosecond laser pulses	4
2.2. Fourier transform pulse shaping	8
2.2.1. General aspects	8
2.2.2. Pulse shaping using liquid crystal spatial light modulators	9
2.2.3. Limitations	12
3. Experimental Setup and Methods	13
3.1. Laser system	13
3.2. Pulse shaping setup	13
3.2.1. Implementation	13
3.2.2. Wavelength calibration	16
3.2.3. Phase calibration	18
3.2.4. Generation of amplitude and phase masks	22
3.3. Pulse characterisation using intensity autocorrelation	23
4. Results and Discussion	25
4.1. Pulse shaper calibration	25
4.1.1. Wavelength calibration	25
4.1.2. Phase calibration	27
4.2. Amplitude shaping	31
4.3. Pulse compression	34
5. Summary and Outlook	38
A. Appendix	40
A.1. Spectral phase expansion coefficients	40
A.2. Pulse shaper transfer function	41
A.3. Pulse shaper dispersion law	42

List of abbreviations

2D	Two-Dimensional
BBO	β -Barium-Borate
CCD	Charge Coupled Device
FROG	Frequency-Resolved Optical Gating
FWHM	Full Width at Half Maximum
GD	Group Delay
GDD	Group Delay Dispersion
GVD	Group Velocity Dispersion
ITO	Indium Tin Oxide
LC	Liquid Crystal
LC-SLM	Liquid Crystal Spatial Light Modulator
NOPA	Non-collinear Optical Parametric Amplifier
PEEM	Photoemission Electron Microscopy
RMSD	Root Mean Square Deviation
SHG	Second Harmonic Generation
SLM	Spatial Light Modulator
SPIDER	Spectral Phase Interferometry for Direct Electric-Field Reconstruction
TA	Transient Absorption

1. Introduction

1.1. Motivation

In 1966, six years after the advent of the laser, the generation of laser pulses with temporal duration on the picosecond scale was reported for the first time by DeMaria et al. [1]. In the following decades, continuous research efforts in the field of laser technology lead to shorter and shorter pulse durations, and today, laser pulses spanning only a few optical cycles are available in various spectral regions [2, 3, 4]. These technical advances paved the way for the development of ultrafast¹ time-resolved spectroscopy techniques such as transient absorption (TA), or pump-probe, spectroscopy which is nowadays routinely employed to investigate dynamic processes triggered by photoexcitation with femtosecond time resolution. The technique has a vast variety of applications, including among others materials science [5] as well as the study of chemical reactions [6] and biological systems [7]. In a generic TA experiment the dynamics of the system under study are investigated in a stroboscope-like manner using two laser pulses (a pump and a probe pulse) with scannable inter-pulse delay. Due to fundamental properties of ultrashort laser pulses, the method suffers from a loss of spectral selectivity for increasingly high temporal resolutions. In the case of systems with a multitude of energy levels in the spectral range of interest, this can lead to congested spectra with overlapping signals that are difficult to disentangle.

In the visible and near-infrared spectral range, these difficulties can be overcome by two-dimensional electronic spectroscopy [8, 9] which simultaneously offers high spectral and temporal resolution. As opposed to a one-dimensional spectrum where the response of a system is mapped to a single frequency-axis, a two-dimensional (2D) spectrum is a function of two frequencies. In short, it contains information about how excitation at one frequency affects the system's response at another (detection) frequency. A schematic spectrum of a simple model system is shown in figure 1.1. In addition to high resolution in both energy and time, 2D spectra have a rich information content that cannot be directly accessed by conventional TA measurements. First, the 2D line shapes give insight into both homogeneous and inhomogeneous broadening and provide a means to access excitation dephasing times [10]. Second, cross-peaks which appear at off-diagonal positions in the spectra provide direct evidence for correlations and/or energy transfer between different energy levels [11]. Exploiting these features, 2D electronic spectroscopy has been used extensively to study energy transport and quantum coherences in photosynthesis [12, 13] and for the study of many-body effects in semiconductor nano-structures [14, 15].

In a typical 2D spectroscopy experiment [16], the sample interacts with a sequence of three laser pulses with variable inter-pulse delays. This results in an optical signal which is fully characterised with respect to amplitude and phase via heterodyne detection, and used later to construct the 2D spectrum. Due to the all-optical character of the method, the attainable spatial resolution is limited to half the excitation wavelength as a consequence of the optical diffraction limit, and 2D spectra therefore represent ensemble averages.

¹Ultrafast spectroscopy techniques make use of *ultrashort* laser pulses, that is, laser pulses shorter than tens of picoseconds, to study dynamics on short time scales (femtoseconds to picoseconds).

However, detection of the optical signal field is not necessarily required. In fact, 2D spectra can be derived from non-coherent signals such as photocurrent [15], fluorescence [17] or photoelectrons [18] that are recorded following the interaction of the sample with the laser pulse sequence. Photoelectrons can be utilized to measure 2D spectra at different locations in a sample with a spatial resolution beyond the optical diffraction limit (referred to as coherent 2D nanoscopy [19]).

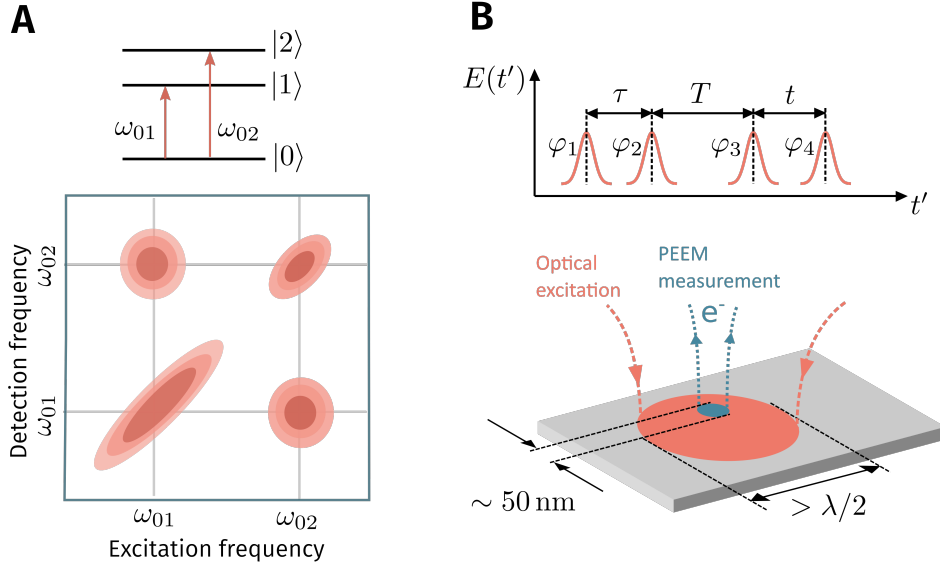


Figure 1.1.: (a): Schematic 2D spectrum (real part) of a simple three-level system. A cut along the diagonal of the spectrum corresponds to the linear absorption spectrum of the system featuring two absorption bands. Off-diagonal cross peaks indicate correlations between energy levels. In this example, cross-peaks occur because there are two allowed transitions sharing the same ground state. (b): Basic principle of coherent 2D nanoscopy. The sample is excited by a four-pulse sequence (shown on top) with variable delays and relative phases. Four pulses are used for excitation because the method relies on non-optical detection. The size of the illuminated area has a lower bound due to the optical diffraction limit. Locally generated photoelectrons are detected with high spatial resolution using PEEM. Figure adapted from [19].

One approach which has been demonstrated in 2011 by Aeschlimann et al. [19] is based on the wide-field detection of photoelectrons using photoemission electron microscopy (PEEM). The basic principle of their method is illustrated in figure 1.1. In short, an optical field consisting of four collinear sub-pulses with controllable delays and relative phases is used to excite the sample. Subsequently, the final state of the sample is probed by detecting locally generated photoelectrons using PEEM. 2D spectra for each spatial location are derived from the local photoelectron-yield as a function of inter-pulse delays and phases. The key point is that photoelectrons can be detected with nanometer spatial resolution due to the small wavelength of electrons [19]. Using this approach, Aeschlimann et al. studied the spatially varying dephasing times of localized plasmon-modes on a corrugated silver surface with 50 nm resolution [19]. Beyond that, their approach opens up possibilities to investigate ultrafast coherent phenomena and electronic couplings in individual nano-objects such as metal or semiconductor nano-structures, molecular aggregates or even single molecules. These studies can be of great relevance for the understanding of fundamental processes on the nanometer spatial and femtosecond time scale, and they are envisioned to play a role in the design of new technologies, for example in the fields of energy harvesting and functional materials [20]

Coherent two-dimensional nanoscopy experiments put high requirements on the laser system. First, the generation of four-pulse sequences with precise control over the inter-pulse delays is required. Furthermore, control over the relative phases of the pulses is necessary because the signal is extracted using phase-cycling techniques originally developed in the context of pulsed NMR spectroscopy [21]. Last, in order to optimise the time resolution of the experiment it is desirable to compress the pulses to the greatest possible extent by compensating for material dispersion in the laser setup. This list of requirements can be met by using Fourier transform pulse shaping [22, 23] - a technique which enables the synthesis of nearly arbitrary temporal waveforms by manipulating input pulses in the frequency domain. In particular, pulse shaping based on liquid crystal spatial modulators as pioneered by Weiner and co-workers in the early nineties [24, 25] has emerged as a widely used tool for shaping of broadband laser pulses. Among other things, the technique is well-suited for dispersion control and the generation of controllable four-pulse sequences for coherent two-dimensional nanoscopy experiments.

1.2. Outline

In this work, a Fourier-transform pulse shaper intended for dispersion compensation and pulse sequence generation for coherent two-dimensional nanoscopy experiments has been implemented and calibrated. The pulse shaper is based on a liquid crystal spatial light modulator, and it is designed for phase and amplitude shaping of femtosecond laser pulses in the visible and near-infrared spectral range. A brief overview on characteristics of femtosecond laser pulses and a short introduction to Fourier transform pulse shaping are given in chapter 2.

To enable accurate shaping of broadband laser pulses, the pulse shaper needs to be calibrated carefully. The design, implementation and validation of a calibration protocol was the centrepiece of the present work. A detailed description of the experimental setup and the calibration procedure is given in chapter 3.

To validate the implemented calibration protocol, calibration results were discussed with regard to consistency and the phase calibration procedure was compared to a standard method described in the literature with respect to data quality and robustness. Additionally, amplitude shaping experiments were carried out where the pulse shaper was used to arbitrarily modulate the spectral amplitude of visible and near-infrared femtosecond pulses. The phase shaping capabilities of the pulse shaper were verified by compensating for phase distortions introduced by strongly dispersive material in the beam path. The outcomes of these investigations are presented and discussed in chapter 4.

Finally, chapter 5 gives a summary of the main findings and discusses possible applications and further development of this work.

2. Background

This chapter briefly discusses the theoretical foundations of the present work. To begin with, section 2.1 reviews the most relevant properties of femtosecond laser pulses with special attention given to the relation between spectral and temporal properties. This sets the stage for a brief introduction to Fourier-transform pulse shaping in section 2.2. Emphasis will be on pulse shaping using liquid crystal spatial light modulators since this technique has been employed in the present work.

2.1. Properties of femtosecond laser pulses

Femtosecond laser pulses can be seen as the coherent superposition of many monochromatic waves with different frequencies. A complete description of a pulse can be given in terms of its electric field $\mathbf{E}(\mathbf{r}, t)$ which is a real-valued vectorial quantity with a spatial and temporal dependence. In this section, however, the discussion will be restricted to linearly polarized laser pulses whose electric field oscillates in a single plane. In addition, the field will be considered at a fixed point in space. Under these assumptions, the laser pulse can be described by a scalar field $E(t)$, which greatly simplifies the discussion. Nevertheless, the features of laser pulses which are most relevant for this work are still captured by the description in terms of the scalar field $E(t)$. If the pulse duration exceeds one optical cycle, which is the case for the pulses used in this work, it is convenient to separate the field $E(t)$ into a temporal envelope $A(t)$ and a rapidly oscillating carrier term:

$$E(t) = A(t) \cos[\phi(t)] = A(t) \cos[\omega_0 t + \phi_{\text{nonlin}}(t)] \quad (2.1)$$

$\phi(t)$ is referred to as the temporal phase of the pulse. Often, it is separated into a linear term $\omega_0 t$, that corresponds to oscillations of the electric field at a centre frequency ω_0 , and a nonlinear term $\phi_{\text{nonlin}}(t)$ which describes temporal variations of the pulse frequency. An important quantity for characterising femtosecond laser pulses is the pulse duration $\Delta\tau$, which is commonly expressed in terms of the full width at half maximum (FWHM) of the temporal intensity $I(t) = |A(t)|^2$.

In the visible and near-infrared spectral range, the electric field oscillates with a frequency at the order of hundreds of THz, and it is therefore impossible to access $E(t)$ directly with present-day's electronics. Often, a spectral representation of the electric field is thus more convenient. Since $E(t)$ is real-valued, its Fourier transform $E(\omega)$ satisfies $E(\omega) = E^*(-\omega)$, and it can therefore be expressed as

$$E(\omega) = E^+(\omega) + (E^+(-\omega))^* \quad \text{with} \quad E^+(\omega) = \begin{cases} E(\omega) & \text{if } \omega \geq 0 \\ 0 & \text{if } \omega < 0 \end{cases} \quad (2.2)$$

Here, the asterisk denotes the complex conjugate. The complex function $E^+(\omega)$, which takes non-zero values only for positive frequencies, contains all information about the temporal pulse shape $E(t)$. Commonly, $E^+(\omega)$ is expressed in terms of the spectral

amplitude $A(\omega)$ and the spectral phase $\phi(\omega)$:

$$E^+(\omega) = A(\omega)e^{-i\phi(\omega)} \quad (2.3)$$

Both the spectral amplitude $A(\omega)$ and phase $\phi(\omega)$ determine the temporal shape $E(t)$ of the pulse, which is given by the real part of the inverse Fourier transform of $E^+(\omega)$:

$$E(t) = 2\Re \left\{ \frac{1}{\sqrt{2\pi}} \int d\omega E^+(\omega)e^{i\omega t} \right\} \quad (2.4)$$

An important quantity, which is related to the spectral phase $\phi(\omega)$, is the group delay $\tau_g(\omega) = d\phi(\omega)/d\omega$. It is defined as the local slope of the phase $\phi(\omega)$, and, at a specific frequency, it can be interpreted as the delay of a narrow-band pulse centred at that frequency. The shortest possible pulse duration for a given amplitude $A(\omega)$ is achieved if the group delay τ_g is constant across the whole laser spectrum, i.e., if $d\phi(\omega)/d\omega = \text{const}$. In this case, the pulse is said to have a flat phase and to be transform limited [23]. Notably, the temporal duration of a transform limited laser pulse is inversely proportional to its spectral width.

If, on the other hand, the spectral phase varies nonlinearly with frequency, severe broadening and distortions of the pulse in the temporal domain can occur [26]. Ultrashort laser pulses are particularly sensitive to this due to their large spectral bandwidth. A common source of nonlinear phase distortions is the dispersion of transparent material (e.g. glass) in the beam path. The effect that propagation through a medium with refractive index $n(\omega)$ has on an ultrashort laser pulse can be described in terms of the phase $\psi(\omega)$ which the pulse accumulates upon propagation through the material:

$$\psi(\omega) = \frac{\omega n(\omega)d}{c_0}. \quad (2.5)$$

c_0 is the speed of light in vacuum and d is the thickness of the material. To further analyse the influence of the spectral phase on the temporal pulse shape, it is convenient to express $\psi(\omega)$ in terms of a Taylor series around the centre frequency ω_0 of the pulse:

$$\psi(\omega) = \psi_0 + \psi_1(\omega - \omega_0) + \frac{\psi_2}{2}(\omega - \omega_0)^2 + \dots + \frac{\psi_n}{n!}(\omega - \omega_0)^n. \quad (2.6)$$

Here, ψ_n denotes the n -th derivative of the phase taken at the centre frequency:

$$\psi_n = \left. \frac{d^n \psi(\omega)}{d\omega^n} \right|_{\omega=\omega_0} \quad (2.7)$$

In most situations, only terms up to third order in the expansion 2.6 have to be retained in order to accurately describe the phase accumulated by femtosecond pulses after transmission through bulk material [26]. The link between the expansion coefficients ψ_n and the refractive index $n(\lambda)$ is discussed in detail in the appendix. The contributions to the phase up to third order influence the laser pulse in a characteristic way. The constant term, ψ_0 , is referred to as absolute phase or carrier-envelope phase. It determines the offset of the electric field oscillations with respect to the pulse envelope. Its influence on the electric field is illustrated in figure 2.1 which shows the field $E(t)$ of an ultra short laser pulse for two different values of ψ_0 . Evidently, the absolute phase has no influence

on the temporal shape of the pulse envelope.

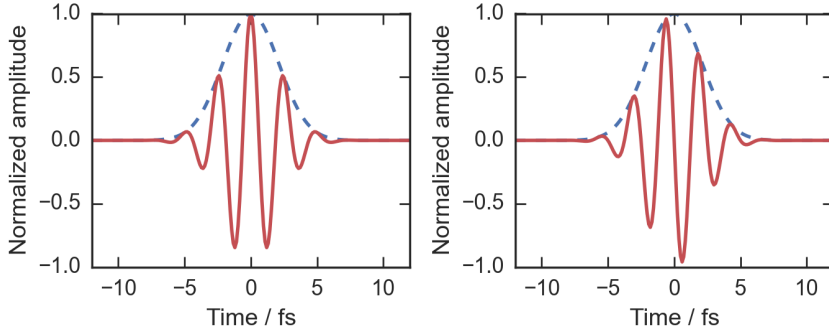


Figure 2.1.: Time dependent electric field $E(t)$ of ultrashort laser pulses with different carrier envelope phases (*left*: $\psi_0 = 0$, *right*: $\psi_0 = \pi/2$). The center wavelength of the pulses is 750 nm and the duration is 5 fs (FWHM).

The first order term, ψ_1 , leads to a constant group delay τ_g and thus simply corresponds to a time shift of the pulse. Just as the carrier-envelope phase, the first order phase ψ_1 does not influence the temporal shape of the pulse envelope.

The term ψ_2 , or group delay dispersion (GDD), describes a quadratic variation of the phase with frequency, which can drastically affect the characteristics and the temporal shape of a femtosecond laser pulse. A quadratic variation of the phase with frequency implies that the group delay $\tau_g = d\psi(\omega)/d\omega$ varies linearly with frequency. As a result, the spectral components of the laser pulse experience different delays, leading to a temporal broadening of the laser pulse. In the temporal domain, a 2nd order phase results in a linear variation of the instantaneous frequency $\omega(t) = d\phi(t)/dt$, which is defined as the time derivative of the temporal phase $\phi(t)$. The pulse is then said to be chirped linearly. In some situations, chirp is purposefully introduced, for example to study light-matter interaction [27, 28] or to achieve high peak powers in chirped-pulse amplification schemes [29]. In ultrafast spectroscopy experiments, on the other hand, chirp is often compensated for to the greatest possible extent to avoid deterioration of the temporal resolution. In the visible and the near-infrared spectral range, most materials show normal dispersion behaviour [26], i.e., the introduced group delay increases with frequency. This results in chirped pulses with the red components in the leading part and the blue frequency components in the trailing part of the pulse.

A purely cubic phase, given by the third order term with coefficient ψ_3 , leads to a series of pre or post pulses in the temporal domain (depending on the sign of ψ_3). In addition, the main pulse experiences temporal broadening, albeit not as pronounced as broadening due to chirp. To illustrate these relations between spectral phase and temporal pulse shape, figure 2.2 shows the spectral and corresponding temporal representation of different pulses.

Temporal pulse broadening after propagation through bulk material is dominated by the GDD. As mentioned above, ultra-short laser pulses are especially sensitive to dispersion due to the large spectral content. As an example, a transform limited pulse centred at 600 nm with an initial duration of $\Delta\tau = 10$ fs will have a duration of about 190 fs after propagating through 10 mm of BK-7 glass which is commonly used in optical components. For a 100 fs long (transform limited) pulse, on the other hand, the same dispersion leads to a final pulse duration of 102 fs, corresponding to an increase of only 2%. This example illustrates the importance of dispersion compensation when working with ultra-short laser

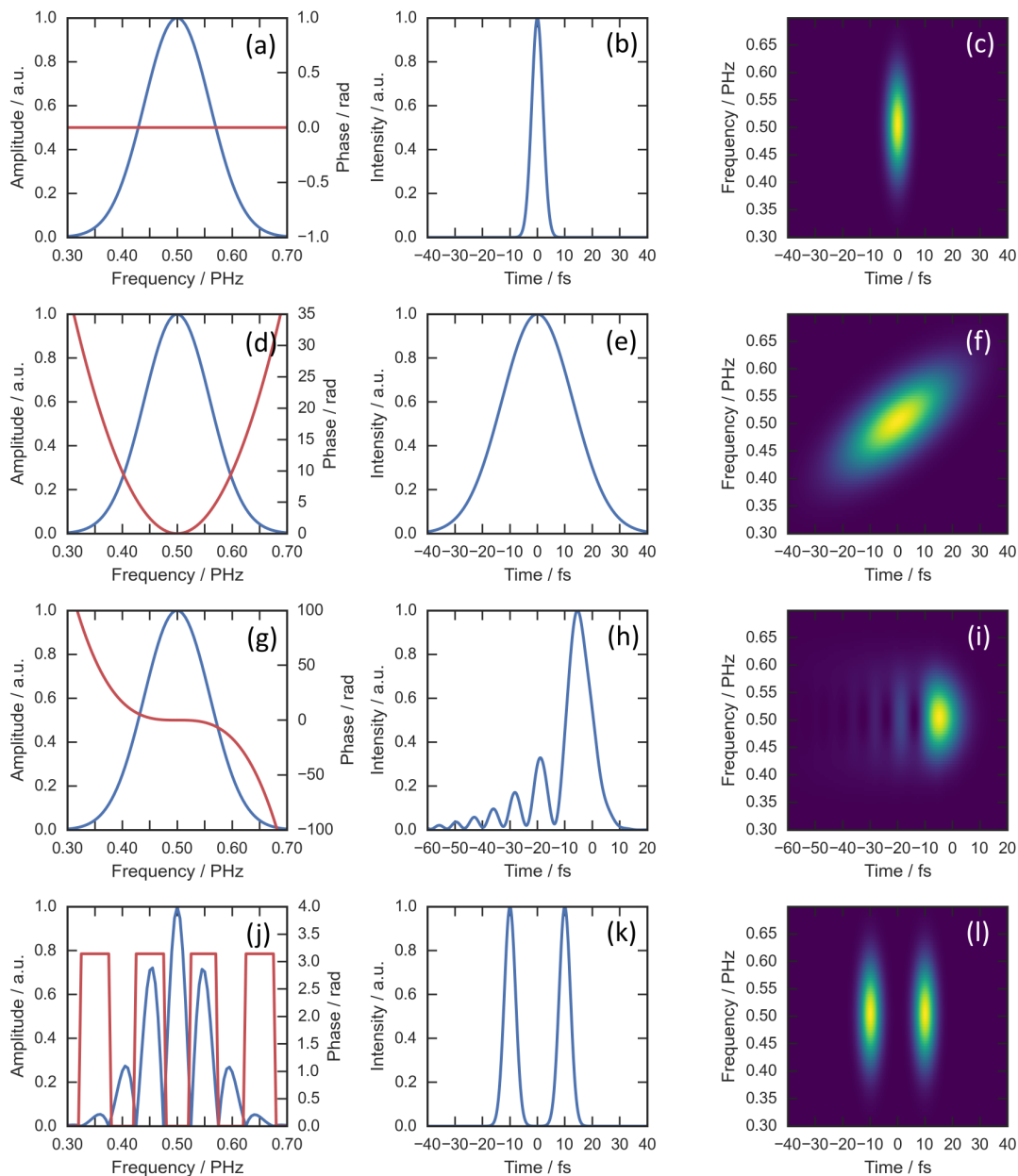


Figure 2.2.: Spectral phase and amplitude (left column), temporal intensity (middle column) and spectrograms (right column) of different pulse shapes. The spectrogram is given by the time-gated power spectrum of the electric field. The following pulses are shown: A transform limited pulse (a-c), a positively chirped pulse (d-f), a pulse with a cubic phase (g-i) and a two-pulse sequence (j-l). The pulses shown in panels (a) to (i) have the same spectral amplitude (centred at 500 THz / 600 nm). The gate functions used for calculating the spectrograms was a Gaussian with the same temporal width as the transform limited pulse (6.2 fs). Figure adapted from [23].

pulses. The GDD introduced by material dispersion can be compensated for using for example pairs of prisms [30], pairs of diffraction gratings [31] or dispersive mirrors such as chirped mirrors [32] or double-chirped mirrors [33]. These components are routinely used in ultrafast optics setups. However, each of these components alone is not suitable for compensating 2nd and higher order phase contributions simultaneously. In addition, changes in the experimental setup require time-consuming realignment. Fourier transform

pulse shaping, on the other hand, is a flexible tool for dispersion control that allows for fast reconfiguration and compensation of 2nd and higher order phases at the same time [34].

2.2. Fourier transform pulse shaping

2.2.1. General aspects

Pulse shaping, i.e., the synthesis of pulses with specific pulse shapes from a given input pulse, is a widely used technique with applications such as pulse compression and dispersion control [34, 35], coherent control of quantum systems [36, 37], bioimaging [38, 39] and multidimensional spectroscopy [19, 40]. Depending on the pulse shaper in use, shaping of spectral phase [25], spectral phase and amplitude [41] or polarization [42] is possible. In this section, the generation of temporal pulse shapes using phase or phase and amplitude shaping will be discussed.

In Fourier transform pulse shaping, the desired waveform $E_{\text{out}}(t)$ is generated by operating on the input pulse in the frequency domain. To this end, the spectral components of the input pulse are separated and manipulated individually by adjusting the component's spectral phase and/or amplitude. Upon recombination, the Fourier components form the shaped output pulse with the desired temporal profile.

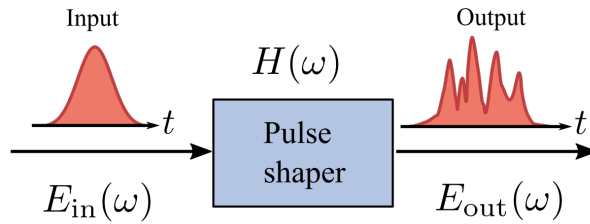


Figure 2.3.: Block diagram representation of Fourier transform pulse shaping. Figure adapted from [43]

In other words, Fourier transform pulse shaping is based on linear, time-invariant filtering in the frequency domain [22], as schematically illustrated in figure 2.3. The action of the pulse shaper on the input field $E_{\text{in}}^+(\omega)$ is given by the complex-valued transfer function $H(\omega)$ and the output field $E_{\text{out}}^+(\omega)$ can be written as

$$E_{\text{out}}^+(\omega) = H(\omega)E_{\text{in}}^+(\omega). \quad (2.8)$$

By analogy with equation 2.3, the transfer function can be expressed as $H = Ae^{-i\phi}$ where A describes amplitude modulation and ϕ is the spectral phase introduced by the pulse shaper. The output field in the time domain can be obtained by simply taking the inverse Fourier transform of $E_{\text{out}}^+(\omega)$:

$$E_{\text{out}}(t) = 2\Re \left\{ \frac{1}{\sqrt{2\pi}} \int d\omega H(\omega) E_{\text{in}}^+(\omega) e^{i\omega t} \right\} \quad (2.9)$$

Experimentally, equation 2.8 is implemented by separating the Fourier components of the ingoing pulse spatially and using a spatial mask for manipulation of spectral phase and amplitude. Subsequently, the spatially separated components are recombined and form a shaped output pulse with a temporal profile according to equation 2.9.

A schematic drawing of the setup most commonly used for Fourier transform pulse shaping, the so-called $4f$ -line [23], is shown in figure 2.4. The spectral components of the incident laser pulse are angularly dispersed by a grating (G) located in the focal plane of a lens (L). The lens recollimates the dispersed input beam and focuses each spectral component on a mask (M), or spatial light modulator (SLM), situated in the rear focal plane of the lens. Here, phase and/or amplitude of the spectral components are manipulated. After traversing the mask, a second lens (L) focuses the light onto another grating (G) where the spectral components recombine.

Notably, the symmetry of the $4f$ -line allows for a folded implementation of the setup where a folding mirror is placed in the centre focal plane of the assembly. This offers the benefit of reduced size and a smaller number of optical components, which facilitates alignment of the setup. In the folded configuration, the SLM is placed directly in front of the folding mirror. The laser pulse thus traverses the SLM twice, thereby increasing the modulation range of the pulse shaper. However, to maintain a good spectral resolution, the mask must be placed within one Rayleigh length from the folding mirror to ensure that the focal spot size at the mask is sufficiently small. This imposes additional constraints on the setup.

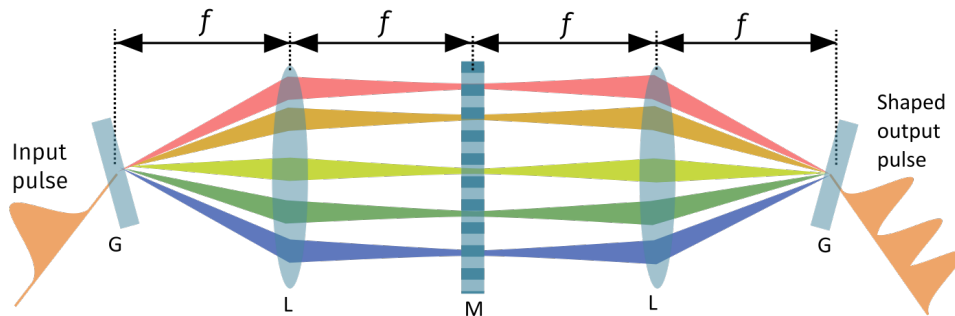


Figure 2.4.: A $4f$ -line for Fourier transform pulse shaping consisting of two gratings (G), two lenses (L) and a spatial mask (M). The spectral components of the ingoing pulse are spatially separated by the first grating before being recollimated and focused onto the mask by the first lens. After the mask, the spectral components are recombined. f is the focal length of the lenses.

2.2.2. Pulse shaping using liquid crystal spatial light modulators

The most commonly used types of spatial masks are acousto-optical modulators and liquid crystal spatial light modulators (LC-SLM) [23]. Both methods have been reviewed extensively [22, 23]. Here, the focus will be on pulse shaping using liquid crystal modulators, a technique which has been pioneered by Weiner and co-workers in the early 1990s [24, 25].

Conceptually, pulse shapers based on LC-SLMs exploit the birefringence of nematic liquid crystals, i.e., the fact that the effective refractive index for an electromagnetic wave traversing the liquid crystal depends on the relative orientation of the liquid crystal (LC) molecules in respect of the polarization and propagation axes of the light wave [24]. Thus, by controlling the orientation of the LC molecules with respect to incident light, it is possible to adjust the effective refractive index. This, in turn, enables control of the spectral phase which is accumulated by the light wave upon travelling through the LC

(see equation 2.5). This is the basis of phase and amplitude shaping using liquid crystal modulators.

The structure of a LC-SLM for phase shaping is depicted in figure 2.5. The SLM consists of a nematic liquid crystal layer which is embedded between two glass slides. The LC mask is subdivided into a linear array of pixels which can be controlled individually using a driving voltage. It is applied via two transparent indium tin oxide (ITO) electrodes which are deposited on the inner surface of the glass slides. The pixels are defined by patterning of one ITO layer into stripe-shaped electrodes, with neighbouring pixels being separated by thin gaps (typically a few μm) in the ITO layer.

Figure 2.5 also shows a sketch of a single LC pixel. When no voltage is applied, the elongated, rod-shaped liquid crystal molecules align along a direction which is dictated by surface patterning of the ITO layer (in this case the x -axis). Following [44], this zero-voltage direction will from now on be referred to as the active axis of the LC mask. In the case of a non-zero driving voltage, the molecules tilt toward the z -axis due to their tendency to align with the electric field. This effectively changes the refractive index n_{eff} for a light wave polarized along the active axis and traversing the pixel in z -direction according to [45]

$$\frac{1}{n_{\text{eff}}^2} = \frac{\cos^2 \theta}{n_o^2} + \frac{\sin^2 \theta}{n_e^2}. \quad (2.10)$$

The angle θ describes the mean orientation of the LC molecules with respect to the z -axis (compare figure 2.5). n_o and n_e denote the ordinary and extraordinary refractive index of the birefringent liquid crystal with $n_e > n_o$ [46]. Notably, the exact relation between driving voltage and the angle θ is not known and has to be calibrated experimentally (see section 3.2.3). It is apparent from equations 2.10 and 2.5 that the spectral phase of a light wave after travelling through the pixel can be controlled via the driving voltage by adjusting the orientation of the LC molecules. In this way, nearly arbitrary phase patterns can be imprinted on the input laser pulse by applying the appropriate voltage pattern to the LC-SLM.

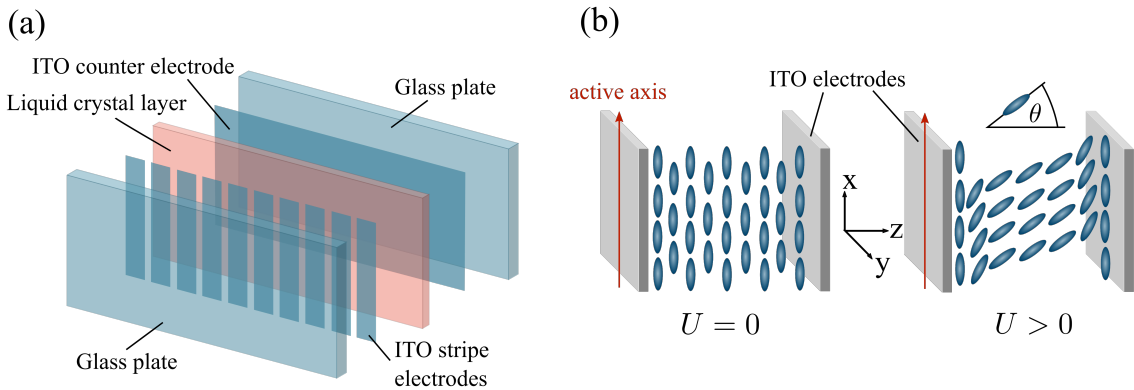


Figure 2.5.: (a) Exploded view drawing of a single liquid crystal mask. The thin liquid crystal layer is embedded between two glass slides. A driving voltage applied via transparent ITO electrodes controls the orientation of the LC molecules. The LC mask is subdivided into several pixels which are defined by gaps between the ITO electrodes. (b) Schematic diagram of a single pixel within the LC display. In the case of no voltage, the LC molecules are aligned along the pixel's active axis which is defined by the surface structure of the ITO layer. A non-zero driving voltage results in a tilt of the LC molecules toward the z -axis. θ denotes the angle between the longitudinal axis of the LC molecules and the z -axis.

Independent shaping of spectral phase and amplitude can be achieved by modifying the arrangement described above [22] as depicted in figure 2.6. The setup now consists of two liquid crystal masks located close behind one another. The active axes of the masks are perpendicular to each other, and at angles $+45^\circ$ and -45° with respect to the x -axis. In addition, polarisers are placed on either side of the dual LC mask.

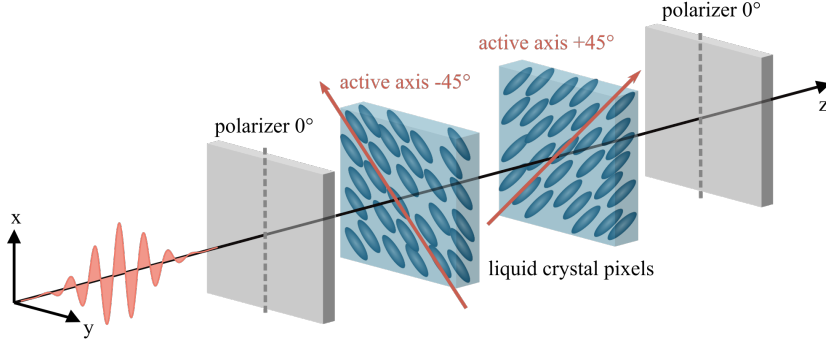


Figure 2.6.: Schematic diagram of a setup for phase and amplitude modulation using a dual LC-mask. Two LC-masks (only a single pixel is shown here) with perpendicular active axis are placed one behind another. The entrance polariser ensures that the incident light is polarised in x -direction, while the exit polariser blocks out the y -component of the field after the second pixel. The sum of the phase shifts introduced by the LC pixels determines phase modulation, while the difference governs amplitude modulation.

The entrance polariser ensures that the input pulse is linearly polarised in x -direction before impinging on the LC mask. On a light wave polarized along the x -direction and propagating along the z -axis, a single LC pixel acts like a programmable waveplate [23]: The wave can be considered to be split into two partial waves which are polarized along the active axis and perpendicular to it, respectively. Propagation through the LC pixel introduces a phase shift $\Delta\phi$ between the partial waves, which is given by

$$\Delta\phi(\omega, U) = \frac{(n_{\text{eff}}(\omega, U) - n_o(\omega))\omega d_{\text{LC}}}{c_0} \quad (2.11)$$

Here, ω is the optical frequency of the light, d_{LC} denotes the thickness of the LC layer and U is the applied driving voltage. n_{eff} is the refractive index governing the propagation of the partial wave polarized along the active axis, as discussed above. $\Delta\phi$ takes its maximum value at zero voltage and decreases monotonically towards higher voltages, as is apparent from equation 2.10. After traversing both pixels and the exit polariser, the output field is given by [22]

$$E_{\text{out}} = E_{\text{in}} \cos\left(\frac{\Delta\phi_1 - \Delta\phi_2}{2}\right) \exp\left(-i\frac{\Delta\phi_1 + \Delta\phi_2}{2}\right) \quad (2.12)$$

E_{in} denotes the amplitude of the input field after the entrance polariser, and $\Delta\phi_1$ and $\Delta\phi_2$ denote the phase shifts introduced by the first and the second pixel, respectively. Equation 2.12 describes an output field that has been manipulated with respect to phase and amplitude. The amplitude modulation is governed by the difference of the phase shifts while the introduced spectral phase is determined by their sum. Sum and difference of the phase shifts can be adjusted independently. The dual LC-mask in combination with two polarisers thus allows for independent shaping of phase and amplitude. A detailed

derivation of equation 2.12 based on Jones calculus is presented in the appendix.

In a $4f$ -line pulse shaper in a folded configuration, the light traverses the LC-SLM twice. To take double-passing through the mask into account, equation 2.12 has to be modified yielding

$$E_{\text{out}} = E_{\text{in}} \cos(\Delta\phi_1 - \Delta\phi_2) \exp(-i(\Delta\phi_1 + \Delta\phi_2)). \quad (2.13)$$

2.2.3. Limitations

Pulse shaping based on LC modulators offers the possibility to synthesize nearly arbitrary waveforms and the technique has been applied in a large variety of experiments. However, accurate pulse shaping is only possible within the limitations of the device, which are mainly due to the pixelation of the LC mask [47]. The subdivision of the LC displays into discrete modulators implies that the pulse shaper can only produce a staircase-function-like approximation to any smooth transfer function $H(\omega)$ [22]. To ensure that the desired transfer function $H(\omega)$ is reasonably well approximated by the LC mask, the phase $\Delta\phi$ must vary sufficiently slowly with respect to pixel position. In other words, the pixel load $\delta\phi$, i.e., the phase difference between neighbouring pixels, must be sufficiently small. More specifically, $\delta\phi$ should satisfy the relation [22]

$$|\delta\phi| \ll \pi \quad (2.14)$$

If the pixel load is comparable to, or greater than, π , the finite spatial extent of the spectral components at the LC-SLM leads to destructive interference between neighbouring pixels. As a consequence, spectral distortions and an overall decrease in pulse energy occur [22, 34]. An experimental demonstration of this effect is given in e.g. in [34] and [41]. Furthermore, a theoretical analysis by Weiner et al. [25] shows that the pixelation gives rise to attenuated and chirped replicas of the main pulse. These replica pulses occur at times $t_{\text{rep}} = n/\delta f$, where δf is the frequency spacing between adjoining pixels and $n \in \mathbb{N}$. Experimentally, these temporal distortions can be countered by weak focusing of the spectrally dispersed input beam onto the mask at the centre of the $4f$ -line. This effectively results in an attenuation of the replica intensity at the cost of decreased spectral resolution and increased interference effects between neighbouring pixels [22]. A good compromise between spectral and temporal distortions can be achieved by choosing a focal spot size slightly smaller than the pixel width [34].

In addition to pixelation effects, the working principle of the $4f$ -line inherently gives rise to an effect referred to as spatio-temporal coupling [23]. As a consequence, shaping of the temporal pulse intensity $I(t)$ results in a change of the spatial properties of the output pulse. A general result is that a programmed time delay of the output pulse leads to a lateral shift of the spatial beam profile [48]. Changes in the overall shape of the spatial beam profile induced by temporal shaping have been observed as well [49]. These effects have to be taken into account in experiments that are sensitive to beam pointing and spatial intensity distribution.

3. Experimental Setup and Methods

In this work a Fourier transform pulse shaper in a folded $4f$ -configuration was implemented. The device is intended to be employed in combination with an amplified, high-repetition rate laser system (section 3.1) in ultrafast spectroscopy and nanoscopy experiments. The pulse shaping setup (section 3.2.1) is based on an LC-SLM which needs to be calibrated in order to perform controlled pulse shaping. First, the spatial dispersion of the pulse shaper needs to be calibrated, i.e., for each SLM pixel the wavelength that impinges on it must be determined (section 3.2.2). Second, the phase shift introduced by the SLM pixels must be calibrated as a function of voltage and wavelength (section 3.2.3). The temporal properties of the output pulses were characterised by means of intensity autocorrelation measurements (section 3.3).

3.1. Laser system

The laser system used in the present work is based on an integrated diode-pumped laser system (*PHAROS, Light Conversion*) delivering pulses with a duration of ~ 170 fs centred at 1028 nm. At full repetition rate (200 kHz), the average output power is 6 W.

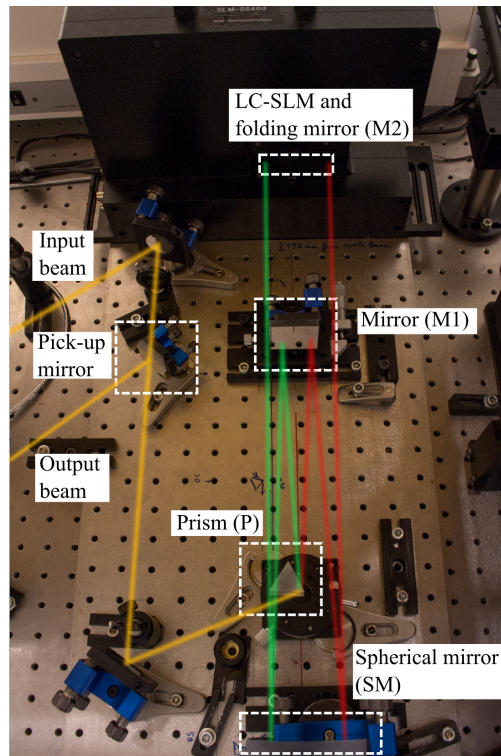
The pulses provided by the *PHAROS* system are used to pump two non-collinear optical parametric amplifiers [50] (NOPAs). In each NOPA, a portion of the input pulse is used for continuum generation in a sapphire crystal [51], yielding a weak pulse featuring a broad and continuous spectrum. A part of this pulse is then amplified using difference frequency generation [52] in a nonlinear β -barium-borate (BBO) crystal. The amplification process is pumped by the 2nd or 3rd harmonic of the fundamental.

By adjusting temporal pulse-overlap and phase-matching conditions in the BBO crystal, amplified broadband pulses with centre wavelengths in the range from 470 nm to 950 nm and spectral bandwidths up to 120 nm can be obtained. A pair of chirped mirrors and/or a prism compressor consisting of two fused-silica prisms in double pass configuration is employed to compensate for the group delay dispersion introduced by optical components in the beam path. At the output, tunable ultrashort pulses (10 fs to 20 fs FWHM) in the visible and near-infrared spectral range with pulse energies up to $1 \mu\text{J}$ are available for spectroscopy experiments.

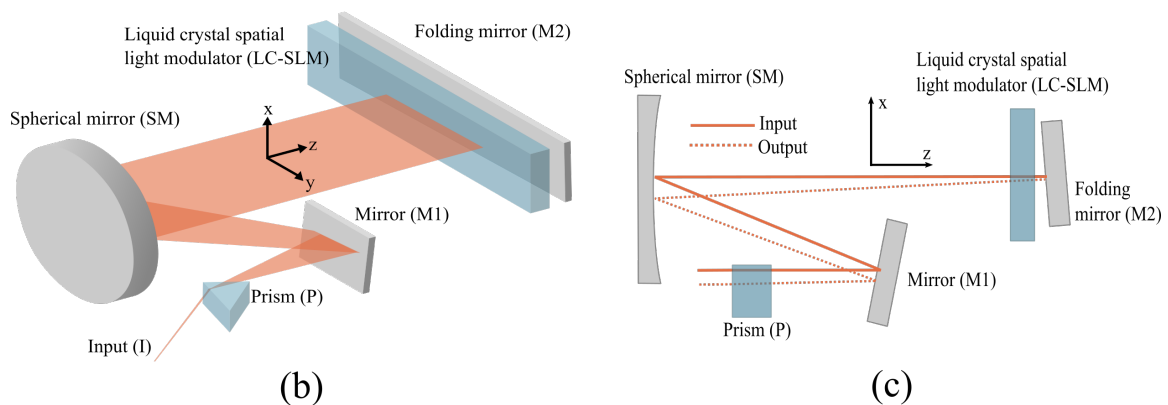
3.2. Pulse shaping setup

3.2.1. Implementation

The pulse shaping setup which was implemented and calibrated in the frame of this work is intended for phase and amplitude shaping of femtosecond laser pulses in the visible and near-infrared spectral range. The setup is arranged in a folded $4f$ -geometry, as discussed in section 2.2. A picture and schematic diagrams of the pulse shaping setup are shown in figure 3.1.



(a)



(b)

(c)

Figure 3.1.: Annotated photograph (a), pseudo 3D-view (b) and side view (c) of the pulse shaper. The incident laser pulse is dispersed by a prism (P) and sent to a spherical mirror (SM) by an intermediate folding mirror (M1). The spherical mirror focuses the light onto the folding mirror M2 which is located directly behind the LC-SLM, in the focal plane of the focusing mirror. The folding mirror (M2) is tilted slightly, such that the outgoing beam is located below the ingoing beam during the second pass through the setup. At the output, the outgoing beam is picked up and sent to the detection system using a pickup mirror.

The incident beam is angularly dispersed by a prism (*Thorlabs, N-SF11 glass*) and sent to a spherical focusing mirror (focal length $f = 50$ cm) via an intermediate folding mirror (M1). Using a spherical mirror instead of lenses for focusing offers the benefit of reduced material dispersion. The path length from the prism apex to the spherical mirror matches the focal length f . The spherical mirror focuses the spectral components of the dispersed beam onto the folding mirror (M2) which is situated directly behind the liquid

crystal spatial light modulator (*SLM-S640d*, *Jenoptik Optical Systems GmbH*). The prism orientation is chosen such that the active area of the LC-SLM covers the spectral range from 470 nm to 980 nm. The centre wavelength, i.e., the wavelength impinging in the centre pixel of the SLM, is 580 nm. As opposed to the arrangement shown in figure 2.13, no entrance polariser is placed in front of the LC-SLM because the laser pulses already are linearly polarized in x -direction when entering the setup. The folding mirror is tilted slightly around the y -axis. Thus, the outgoing beam travels below the ingoing beam during the second pass through the setup which is illustrated in panel (c) of figure 3.1. After the spectral components are recombined in the prism, the output pulse is sent to the detection system. The exit polariser (compare figure 2.13) is placed after the pickup mirror.

The spatial light modulator used in this setup is designed for phase and amplitude shaping of light in the range from 430 nm to 1600 nm with a maximum phase change between 7π (430 nm) and 2π (1600 nm) for a single pass [46]. The device consists of two pixelated liquid crystal masks with an active area of $64 \times 10 \text{ mm}^2$, situated directly behind one another. Each mask consists of a thin layer of nematic liquid crystal ($10 \mu\text{m}$ thickness) which is embedded between two glass slides. The masks are subdivided into a linear array of 640 pixels, which, in turn, are $97 \mu\text{m}$ wide and separated by gaps of $3 \mu\text{m}$. The pixels of each mask can be controlled individually by means of a driving voltage that is applied via two transparent indium tin oxide (ITO) electrodes. The voltage level can be set with 12 bit resolution. A section view of the dual LC mask is shown in figure 3.2.

The displays can be operated in two modes. In the high-voltage mode, the driving voltage ranges from 0 V to 8 V while the maximum voltage in the low-voltage mode is 5 V. In this report, the driving voltages are typically not given in units of volt but in terms of a driving level ranging from 0 d.u. (digital units) to 4095 d.u. with a driving level of 4095 d.u. corresponding to the maximum voltage. In all experiments, the LC-SLM was operated in the high-voltage mode.

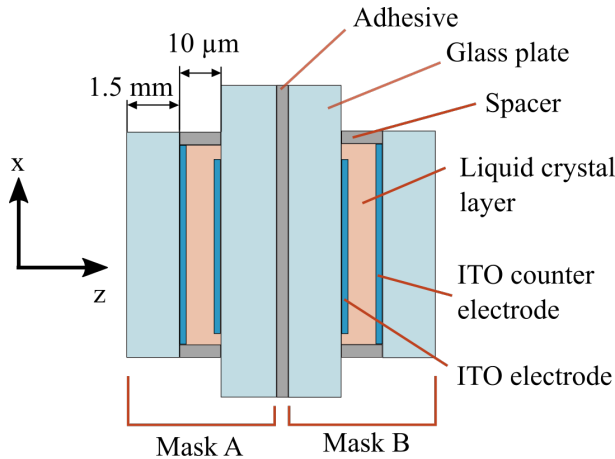


Figure 3.2.: Section view of the dual LC mask.

The major difference between the pulse shaping assembly described above and the commonly used $4f$ -line presented in section 2.2 is the use of a prism in place of a grating to angularly disperse the ingoing beam. The advantage of gratings over prisms is that the former offer strong angular dispersion without introduction of additional material dispersion [34]. However, gratings typically exhibit a low diffraction efficiency over large bandwidths ($< 50\%$) [34]. This severely limits the throughput of the pulse shaper if

used for shaping of pulses with a very broad spectrum or tunable centre wavelength. Additionally, if the bandwidth of the pulses exceeds one octave, consecutive diffraction orders start to overlap. In this case, the spectral components of the pulse cannot be addressed individually by the SLM and controlled pulse shaping is not possible any more [34].

Brewster prisms, on the other hand, offer the benefit of high and uniform transmittance over the whole visible and near-infrared spectral range. Moreover, the bandwidth is not limited to one octave since prisms refract every spectral component into a single, distinct direction. However, to make use of the whole active area of the LC-SLM while keeping the setup reasonably compact, strong angular dispersion of the incident beam is necessary. This, in turn, requires a prism consisting of highly dispersive material. As a consequence, pulses passing through the setup are subject to strong material dispersion and undergo severe temporal broadening. This has to be compensated for additionally.

To minimise material dispersion introduced by the prism, it is desirable to reduce the distance which the pulses are travelling in the prism as much as possible by positioning the beam close to the prism apex. However, a lower limit for this distance is imposed by the diameter of the incident beam and the requirement that significant energy losses due to beam clipping at the prism edge should be avoided. In addition, a relatively large beam diameter at the prism is required since the focal spot size at the LC-SLM should be slightly smaller than the pixel width (100 μm in this setup, see section 2.2). According to reference [34] where a similar LC-SLM was used, a beam waist of 90 μm in the focal plane is a good compromise between spectral and temporal distortions. For a pulse in the visible spectral range centred at 550 nm and a focal length $f = 50$ cm, this requires a beam diameter of about 4 mm at the prism. Consequently, double passing through the pulse shaping assembly introduces a GDD of approximately 2400 fs². This includes material dispersion introduced by the glass windows¹ of the LC-SLM. The path length in the prism was estimated assuming minimum deviation conditions and a distance of one beam radius between the centre of the beam and the prism apex. Similar considerations for a near-infrared pulse centred at 750 nm give a GDD of 1640 fs². Notably, the phase distortions are more severe for the pulse centred at 550 nm because the group velocity dispersion² (GVD) of glasses typically increases towards lower wavelengths. As a consequence, a substantial amount of GDD plus higher order phase contributions have to be compensated for. In principle, this can be achieved using the phase shaping capabilities of the pulse shaper. However, compensating a GDD as high as 1640 fs² or 2400 fs² requires a large pixel load $\delta\varphi$ and thus results in spectral distortions of the output pulses. Therefore, a prism-compressor consisting of two fused-silica prisms in double pass configuration was used for dispersion compensation in this work.

3.2.2. Wavelength calibration

The aim of the wavelength calibration is to determine the pixel-to-wavelength mapping of the pulse shaper. In principle, this relation can be derived directly from the dispersion law of the pulse shaper which describes the lateral displacement $p(\lambda)$ at the the SLM as a function of wavelength:

$$p(\lambda) - p_0 = \eta f \tan \left[\beta - \frac{\pi}{2} + \arcsin \left(\sqrt{n(\lambda)^2 - \sin^2(\theta_i)} \sin(\alpha) - \sin(\theta_i) \cos(\alpha) \right) \right] \quad (3.1)$$

¹For the calculations, it was assumed that the window material is fused silica.

²The group velocity dispersion can be defined as the introduced GDD per unit length.

Here, p_0 is the centre pixel of the SLM, $\eta = 10/\text{mm}$ is the density of pixels, f is the focal length of the focusing mirror, α is the apex angle of the prism, θ_i is the angle of incidence at the prism and β describes the orientation of the prism with respect to the SLM. $p(\lambda)$ gives the displacement in units of pixels. The wavelength dependence of $p(\lambda)$ is entirely contained in the refractive index $n(\lambda)$ of the prism material [53]. The derivation of equation 3.1 is given in the appendix A.3. All quantities that determine $p(\lambda)$ are known or can be measured in the setup. In practice, however, $p(\lambda)$ is extremely sensitive to errors in the angles θ_i and β which can only be measured with limited accuracy.

This limitation can be overcome by measuring $p(\lambda)$ for a number of wavelengths across the laser spectrum. These reference points are then used to fit the model given in equation 3.1. To measure $p(\lambda)$, a single pixel k of the SLM is programmed to have low transmittance while the remaining pixels are deactivated by applying the maximum driving voltage, resulting in high transmittance at these pixels. This configuration results in a sharp dip in the transmission spectrum of the SLM at the centre wavelength of the dark pixel. This can be seen in figure 3.3. Fitting a Gaussian or second order polynomial to the data in the vicinity of the minimum yields the centre wavelength λ_k of the k th pixel.

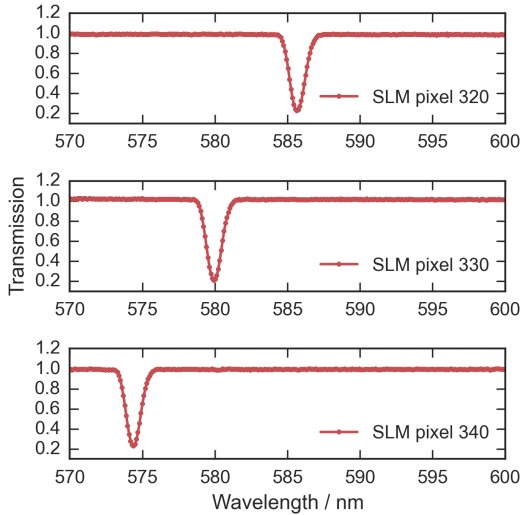


Figure 3.3.: Three transmission spectra of the SLM. The transmittance of a single pixel has been lowered while the remaining pixels have been deactivated (i.e. no attenuation) by applying the maximum driving voltage. This configuration results in a distinct dip in the transmission spectrum located at the centre wavelength of the dark pixel.

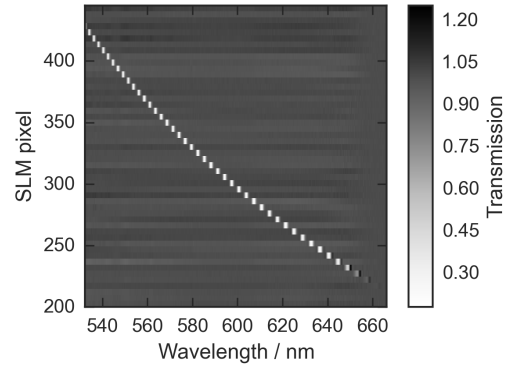


Figure 3.4.: A set of SLM transmission spectra plotted as a heatmap. Each horizontal line represents a colour-coded transmission spectrum. The position of the dark pixel is given on the vertical axis.

Measuring several transmission spectra while scanning the position of the dark pixel gives the displacement $p(\lambda)$ at several points. A complete dataset recorded for this purpose is presented in figure 3.4, which clearly shows the non-linear variation of centre wavelength with pixel number. Subsequently, equation 3.1 is fitted to the measured displacement starting from a rough estimate for θ_i and β . In addition, the SLM is assumed to be perfectly centred which implies $p_0 = 320$. The fitting gives the displacement $p(\lambda)$. The final step is to invert the optimised model numerically to determine the centre wavelengths of all 640 SLM pixels. The resulting calibration curve $\lambda(k)$, i.e., the centre wavelength as a function of pixel number k , is saved as a textfile for later use.

Notably, the wavelength calibration procedure described above requires a well-calibrated spectrometer to correctly assign the centre wavelengths. In this work, a spectrograph (*SpectraPro 2300i*, Princeton Instruments) equipped with a CCD camera (*PIXIS 100*, Princeton Instruments) was used for spectral intensity measurements. The spectrometer was calibrated using the emission lines from a neon lamp as reference. In addition, the spectral resolution of the CCD camera must be at least the same as the spectral resolution of the pulse shaper to unambiguously map wavelengths to pixels. The average frequency spacing $\delta\nu_{\text{SLM}}$ between the SLM pixels is 0.5 THz while the CCD pixels are separated by approximately $\delta\nu_{\text{CCD}} = 0.08$ THz, well below $\delta\nu_{\text{SLM}}$. The spectrometer used in the present work is thus able to resolve individual SLM pixels. This is demonstrated in figure 3.5 which shows two transmission spectra of the SLM with the 50th and 51st pixel set to low transmittance, respectively. The two dips are clearly shifted with respect to each other, indicating that the wavelength-to-pixel mapping can be determined unambiguously.

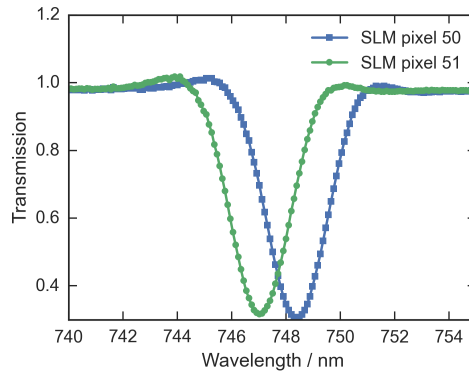


Figure 3.5.: Transmission spectra of the SLM with the 50th and 51st pixel set to low transmittance. The shift between the spectra is clearly resolved by the CCD camera.

Within the frame of this project, all steps required to perform a wavelength calibration as outlined above, that is, data acquisition and evaluation, were implemented using the *LabVIEW* development environment.

3.2.3. Phase calibration

Overview

The second part of the calibration is to determine the introduced phase shift $\Delta\varphi(U, \lambda)$ as a function of driving voltage U and wavelength λ for both LC masks. The phase calibration procedure implemented in this work retrieves the phase $\Delta\varphi(U, \lambda)$ indirectly from an *in situ* measurement of the wavelength and voltage dependent intensity modulation of the pulse shaper. Other calibration approaches which directly measure the phase using interferometry have been demonstrated [54, 55], but they require a separate calibration setup. The indirect method, on the other hand, can be carried out in the pulse shaping setup and therefore inherently takes influences of the alignment into account [56]. At a specific wavelength λ_0 , the intensity modulation $T = I/I_0$ of the pulse shaper, i.e. the ratio of transmitted to initial intensity, is given by

$$T_{\lambda_0}(U_1, U_2) = \cos^2(\Delta\varphi_1(U_1, \lambda_0) - \Delta\varphi_2(U_2, \lambda_0)). \quad (3.2)$$

$\Delta\varphi_1$ and $\Delta\varphi_2$ are the phase shifts introduced by the first and the second LC display, respectively, by applying the driving voltages U_1 and U_2 . It is clear from equation 3.2 that the intensity modulation depends on the phase shifts introduced by both LC masks. To decouple the calibration of the masks to the greatest possible extent, the maximum driving voltage is applied to all pixels of one mask (henceforth referred to as the inactive mask). This reduces the phase shift introduced by the inactive mask to approximately zero, effectively setting the mask to an optically inactive state [46]. As a consequence, the influence of the inactive mask on the amplitude modulation can be neglected to a good approximation [46] and equation 3.2 can be simplified to

$$T_{\lambda_0}(U) = \cos^2(\phi(U, \lambda_0)) \quad (3.3)$$

where $\phi(U, \lambda_0)$ now denotes the voltage dependent phase shift introduced by the active mask. The phase ϕ can be retrieved by inverting equation 3.3 - this will be discussed further below. In theory, the full wavelength dependence of $\phi(U, \lambda)$ can be captured by determining the voltage dependent phase shift at a single wavelength λ_0 and extrapolating to other wavelengths [23] using the relation

$$\phi(U, \lambda) = \phi(U, \lambda_0) \frac{\lambda_0}{\lambda} \frac{\Delta n(\lambda)}{\Delta n(\lambda_0)}. \quad (3.4)$$

Here, $\Delta n(\lambda)$ is the wavelength dependent birefringence of the LC modulators which is provided by the manufacturer in terms of a Sellmeier-equation [46]. This approach is suggested by the manufacturer and it has been used for example in reference [34]. In this work, however, a broadband calibration procedure was implemented, i.e., the dispersion of $\phi(U, \lambda)$ was determined directly by calibrating the SLM pixels independently and at their centre wavelengths. This approach has the advantage that deviations from the ideal behaviour and inhomogeneities among the pixels are taken into account.

To measure the wavelength and voltage dependent intensity modulation for phase retrieval, one LC mask is deactivated as described above while a uniform driving voltage U is applied to all pixels of the active mask and scanned from minimum to maximum voltage. For each voltage setting, the spectral intensity $I(\lambda)$ of a broadband laser pulse after travelling through the pulse shaper is measured. This gives a spectrogram $I(U, \lambda)$ as shown in figure 3.6. At each wavelength, the intensity oscillates between a maximum value and approximately zero, with the oscillation period increasing from lower to higher voltages. This can also be seen in figure 3.7 where a cut of the spectrogram along the voltage axis is shown. Due to the wavelength dependence of the phase shift $\phi(U, \lambda)$ the extrema of $I(U, \lambda)$ do not occur at the same voltage values, but along tilted lines. In addition to the voltage-dependent intensity modulation, a sinusoidal modulation is superimposed on the spectra $I(\lambda)$ at certain voltages (visible as vertical stripes in figure 3.6). This distortion, which originates from a Fabry-Pérot effect inside the SLM, is discussed in detail in the results part of this report.

After data acquisition, the phase shift $\phi(U, \lambda)$ of the active mask is retrieved using an evaluation procedure that can be divided into the following steps:

- i) **Data selection:** A certain wavelength range is manually specified such that all intensity traces $I_\lambda(U)$ (horizontal lines in the spectrogram) within that range feature clear modulations with reasonable signal-to-noise ratio.
- ii) **Phase extraction:** The phase ϕ is retrieved separately from every intensity trace

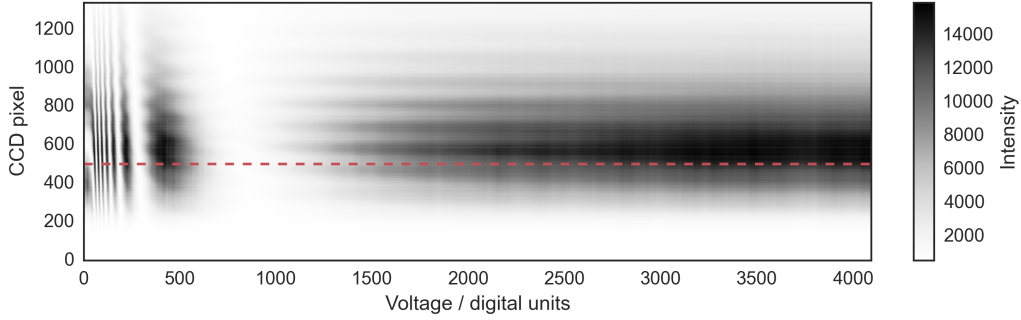


Figure 3.6.: Spectrogram measured for the phase calibration of the SLM with mask B as the active mask. The intensity oscillates with the driving voltage with the oscillation frequency increasing towards lower voltages. In addition, a sinusoidal modulation of the intensity occurs at certain driving voltages.

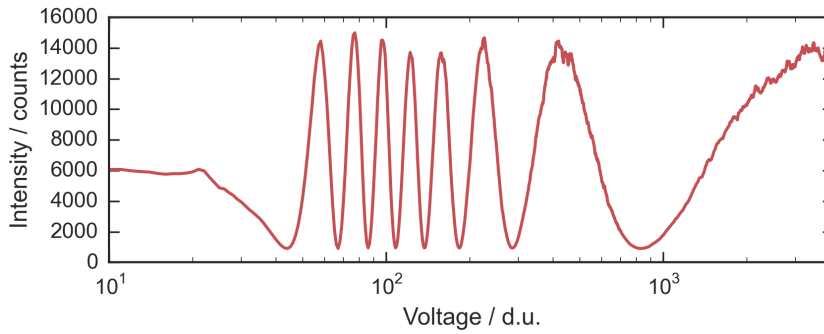


Figure 3.7.: Voltage dependent intensity after transmission through the SLM for a single wavelength. (Corresponds to the red dashed line in figure 3.6.)

$I_\lambda(U)$ within the specified range. This gives the voltage and wavelength dependent phase $\phi(U, \lambda)$ of the active mask.

iii) Noise reduction: As a last step, noise in $\phi(U, \lambda)$ is removed by Gaussian filtering.

These steps result in a smooth and continuous function $\phi(U, \lambda)$ describing the phase shift of the active mask. Repeating the whole procedure with the roles of the active and inactive mask changed gives the phase for both LC masks. Finally, the voltage and wavelength dependent phase of each LC mask is saved as a separate calibration file. A more detailed description of steps **ii** and **iii** as outlined above will be given in the following. A *LabVIEW* program which controls data acquisition and processing for phase calibration runs has been developed within the context of this project.

Phase extraction from a single intensity trace

The voltage dependent phase shift $\phi(U, \lambda_0)$ at a specific wavelength λ_0 is encoded in the shape of the intensity trace $I(U)$ at that wavelength. This is described by equation 3.3 and the phase can be retrieved by inverting this relation.

As a first step, the intensity trace $I(U)$ needs to be brought into a shape that is consistent with equation 3.3, i.e., the intensity needs to be normalised such that it oscillates between zero and unity. To this end, the intensity trace is normalised using linear segments through its minima and maxima as lower and upper normalisation boundary, respectively. This is illustrated in figure 3.8. This procedure ensures that the normalised data is zero

(unity) at all minima (maxima). Typically, this cannot be achieved by simply normalising $I(U)$ with respect to its global maximum since noise in the data gives rise to fluctuations in the intensity at the local extrema.

After normalisation, the phase can be calculated by directly inverting equation 3.3 which gives

$$\phi(U, \lambda_0) = k\pi \pm \arccos \sqrt{T(U)}. \quad (3.5)$$

Here, $T(U)$ denotes the normalised intensity trace and k is an integer number. The term $k\pi$ appears because a periodic function cannot be inverted unambiguously: relation 3.3 remains valid if a multiple of π is added to the phase ϕ . For phase retrieval, the intensity trace is subdivided into intervals with the interval boundaries given by the position of the extrema of $I(U)$. In each interval, the phase is calculated using the relation displayed above with the value of k and the sign of the arccos function chosen such that the resulting phase curve is continuous and monotonically falling over the whole voltage range. These constraints are imposed to take the working principle of the LC-SLM into account. The normalisation of the intensity trace ensures continuity at the interval boundaries where pieces of the phase curve are stitched together. A phase curve that was obtained in this way and the corresponding intensity trace are shown in figure 3.9.

This direct method for phase retrieval is easy to implement and reliably produces continuous and smooth phase curves if the noise level is very low. In practice, however, noise distorts the intensity traces in particular in the vicinity of the local maxima. Here, the inversion procedure is particularly sensitive to noise because the derivative of the arccos function diverges if its argument approaches unity. As a result, the phase curves can be severely distorted and exhibit jumps at the maxima of $I(U)$ [23, 56]. In addition, the direct phase retrieval hinges on an accurate detection of the minima and maxima of $I(U)$, which is also hampered by the presence of noise around the extrema.

To overcome these problems, a two-step method for phase retrieval was implemented in the frame of this work. As a first step, the direct method described above is used to calculate the phase at several points across the whole voltage range. The phase is then expressed in terms of natural cubic spline interpolation [57] of these control points. Second, using a stochastic optimisation algorithm the control points are adjusted such that the phase, expressed as a natural cubic spline, reproduces the normalised intensity trace. To this end, the optimisation procedure minimises the root-mean-square-deviation (RMSD) between the normalised intensity $T(U)$ and the squared cosine of the phase (compare equation 3.3), with the RMSD given by

$$\text{RMSD} = \sqrt{\sum_i^N [T(U_i) - \cos^2(\phi_{\text{Spline}}(U_i))]^2 / N}. \quad (3.6)$$

The sum runs over all voltage values U_i where the intensity has been measured and ϕ_{Spline} denotes the cubic spline representation of the phase. The optimisation algorithm used here corresponds to the simulated annealing algorithm [58] at zero temperature, i.e., at every iteration the control points are changed randomly and only changes that reduce the RMSD are accepted. Despite the simplicity of the algorithm, the method converges in the vast majority of cases because the initial guess obtained from direct phase retrieval already reproduces the normalised intensity reasonably well.

For the initial guess, control points are initialised at the positions of local intensity extrema, and at minimum and maximum voltage. At a later stage during the optimisation,

the number of control points is doubled to further refine the phase curve, resulting in 30 to 40 control points in total. This number is much smaller than the length of a typical intensity trace (~ 1000 points) and the spline optimisation therefore captures the crucial features of $T(U)$ but the rapidly fluctuating noise contributions are effectively averaged out.

The resulting phase curves $\phi(U)$ are free of distortions over the whole voltage range and accurately reproduce the measured normalised transmission (see chapter 4).

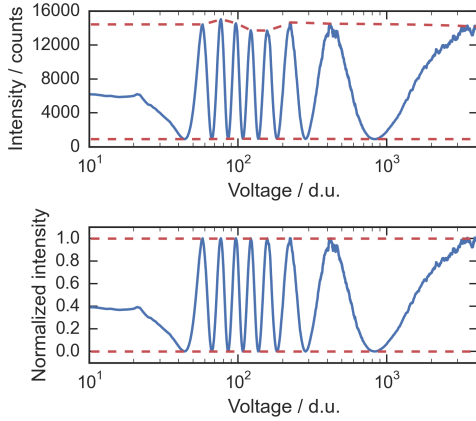


Figure 3.8.: *Top:* Intensity trace before normalisation. For normalisation, linear interpolation of the maxima and minima is used to get the upper and lower normalisation boundary, respectively (red dashed lines). *Bottom:* After normalisation, the intensity oscillates between zero and unity.

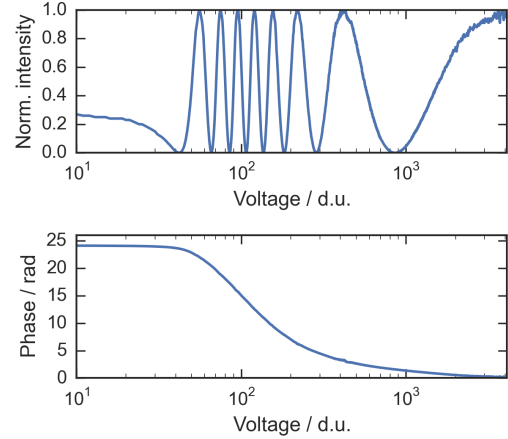


Figure 3.9.: *Top:* Normalised intensity trace. *Bottom:* Phase curve extracted from the intensity trace in the top panel using the direct inversion approach outlined in the text.

Noise reduction

The phase extraction procedure outlined above ensures that, at any wavelength, the phase is continuous and noise free over the whole voltage range. However, since the phase curves at different wavelengths are determined independently and due to the stochastic nature of the algorithm for phase retrieval, the phase as a function of wavelength at a given voltage, $\phi(U_0, \lambda)$, is to a certain degree distorted by noise, as shown in figure 3.10. To compensate for this, Gaussian filtering is used which efficiently suppresses the high frequency noise, as shown in figure 3.10. After noise reduction, the phase $\phi(U, \lambda)$ is distortion free with respect to both wavelength and voltage.

3.2.4. Generation of amplitude and phase masks

Once both wavelength and phase calibrations have been obtained, the resulting calibration functions can be applied to generate the voltage patterns required to realise a given transfer function $H(\lambda)$. In the general case, H describes both amplitude and phase modulation with

$$H(\lambda) = A(\lambda)e^{-i\psi(\lambda)}. \quad (3.7)$$

$A(\lambda)$ describes amplitude modulation whereas $\psi(\lambda)$ denotes the added spectral phase. The first step is to evaluate the transfer function at every pixel's centre wavelength,

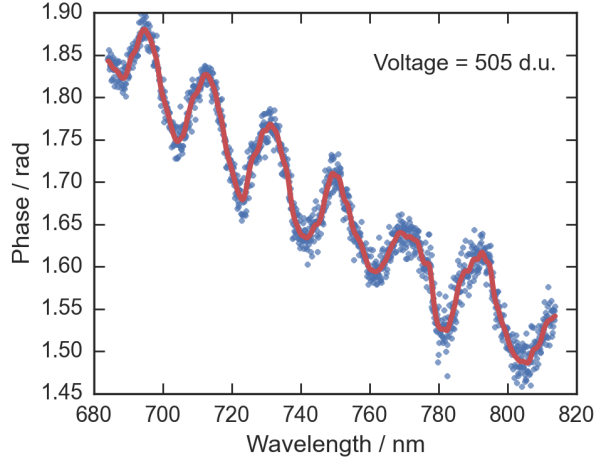


Figure 3.10.: Phase as a function of wavelength at a driving voltage $U = 505$ d.u. before (blue dots) and after (red solid curve) Gaussian filtering for noise reduction.

which is given by the wavelength calibration. Next, the appropriate driving voltages U_A and U_B for mask A and B have to be determined at every pixel. For a given pixel with centre wavelength λ_0 , the phase shifts $\Delta\phi_A$ and $\Delta\phi_B$ which are required to achieve the desired amplitude and phase modulation are given by

$$\begin{aligned}\Delta\phi_A(U_A, \lambda_0) &= \frac{\psi(\lambda_0)}{2} + \frac{\arccos A(\lambda_0)}{2} \\ \Delta\phi_B(U_B, \lambda_0) &= \frac{\psi(\lambda_0)}{2} - \frac{\arccos A(\lambda_0)}{2}.\end{aligned}\tag{3.8}$$

It is apparent from equation 2.13 that these settings for $\Delta\phi_A$ and $\Delta\phi_B$ result indeed in the desired modulation behaviour. As a result of the phase calibration, $\Delta\phi_A$ and $\Delta\phi_B$ are given as (tabulated) functions of driving voltages U_A and U_B , respectively, at the pixel's centre wavelength λ_0 . Thus, to derive the appropriate voltages, the relations displayed above in equation 3.8 can be solved numerically for U_A and U_B . Repeating this for every SLM pixel gives the voltage patterns that need to be applied to mask A and B to realise the desired transfer function H .

3.3. Pulse characterisation using intensity autocorrelation

Tools for characterising femtosecond laser pulses with respect to pulse shape and duration are indispensable for measuring and compensating for dispersion effects. Measuring the temporal pulse shape $I(t)$ is particularly challenging because pulse durations of ultra-short laser pulses are orders of magnitude below the response times of the fastest electronic photodetectors [26]. Several techniques have been developed to retrieve the spectral phase and amplitude of a laser pulse, which enables the reconstruction of the time dependent intensity $I(t)$. The most prominent examples of these techniques are *frequency-resolved optical gating* (FROG) [59] and *Spectral phase interferometry for direct electric-field reconstruction* (SPIDER) [60].

Another approach, which was used in this work, is intensity autocorrelation. This

technique allows for the measurement of the autocorrelation function $R(\tau)$ of the temporal intensity which is given by

$$R(\tau) = \frac{\langle I(t)I(t - \tau) \rangle}{\langle I(t)^2 \rangle}. \quad (3.9)$$

In contrast to FROG and SPIDER, the method yields only partial information about the intensity $I(t)$ and additional assumptions about the pulse shape have to be made in order to extract the pulse duration $\Delta\tau$. Commonly, $I(t)$ is assumed to have a Gaussian or a sech^2 -shape. Since the resulting value for $\Delta\tau$ depends on the choice of the reference shape, pulse durations obtained using the autocorrelation technique have to be interpreted carefully. Experimentally, the autocorrelation function can be measured using the setup shown in figure 3.11 on the left hand side. The ingoing laser pulse is split into two replicas and one of the replicas is delayed with respect to the other by a time τ using a delay line. The two replicas are then focused onto a thin crystal with a $\chi^{(2)}$ non-linearity. Here, second harmonic generation (SHG), i.e., the generation of light at twice the input frequency, occurs and the second harmonic signals emerge in three phase matching directions \mathbf{k}_1 , \mathbf{k}_2 and $\mathbf{k}_1 + \mathbf{k}_2$. \mathbf{k}_1 and \mathbf{k}_2 are the wave vectors of replica 1 and replica 2 respectively. The signal propagating along $\mathbf{k}_1 + \mathbf{k}_2$ is created in a two-photon process involving both replica 1 and replica 2, and its strength therefore depends on the temporal overlap of the replicas. It is isolated using a spatial mask and sent to a photodiode that is used to measure its time averaged intensity $\langle I_{SHG} \rangle$. Measuring $\langle I_{SHG} \rangle$ as a function of the inter-pulse delay τ yields the correlation function $R(\tau)$. Finally, the pulse duration $\Delta\tau$ is obtained from the FWHM of the autocorrelation trace $R(\tau)$ by multiplication with $1/\sqrt{2}$, which is based on the assumption that the pulse has a Gaussian shape.

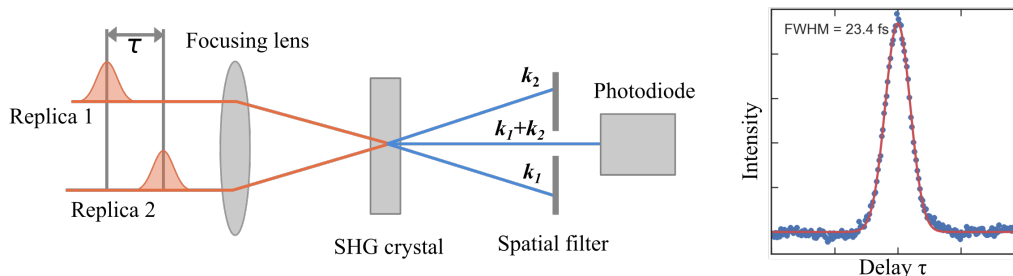


Figure 3.11.: Schematic diagram of a setup for intensity autocorrelation of femtosecond laser pulses. The ingoing pulse is split into two replica (not shown) and one replica is delayed by a time τ in respect of the other. The two pulse replicas are then focused onto a non-linear crystal where second harmonic generation occurs. The second harmonic signals emerge in three phase matching directions. Using a spatial filter, the signal depending on the temporal overlap of the replicas is selected and sent to a photodiode. The time-average of this signal gives the autocorrelation of the pulse's temporal intensity $I(t)$. A typical result is shown on the right hand side. The pulse duration $\Delta\tau$ can be estimated from the autocorrelation trace.

4. Results and Discussion

4.1. Pulse shaper calibration

4.1.1. Wavelength calibration

Results of wavelength calibrations using pulses in the visible and near-infrared spectral range are displayed in figures 4.1 and 4.2 which show the measured lateral displacement at the LC-SLM as a function of wavelength and the fitted model. In both spectral regions, the agreement between the fitted model and the measured data is excellent. This confirms the validity of the wavelength calibration procedure. Figure 3.5 shows a plot of the calibration curve, i.e., the pixel-to-wavelength mapping, extracted from the fit shown in figure 4.2. Due to the non-linear angular dispersion of the prism, the centre wavelength varies non-linearly with the pixel number with the wavelength spacing between adjoining SLM pixels decreasing from 1.8 nm at the red edge (~ 830 nm) to about 0.2 nm at the blue edge (~ 450 nm) of the spectral range covered by the LC-SLM. Correspondingly, the frequency spacing changes from 0.8 THz to about 0.3 THz (compare figure 4.3). This implies that the spectral resolution of the LC-SLM increases towards lower wavelengths, which, in turn, affects phase shaping limits of the setup as discussed in the following.

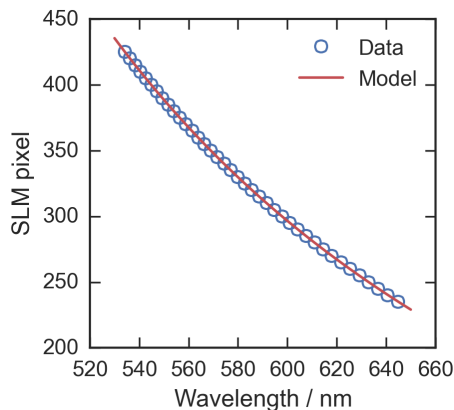


Figure 4.1.: Displacement at the SLM measured as a function of wavelength in the visible spectral range and fitted model.

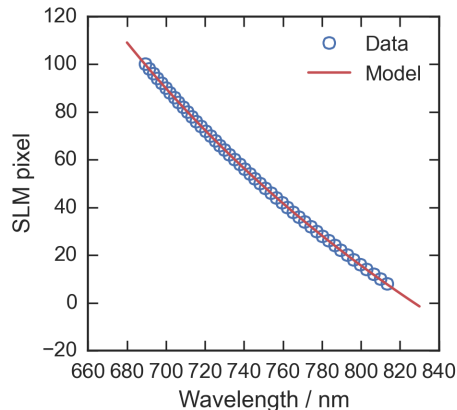


Figure 4.2.: Displacement at the SLM measured as a function of wavelength in the near-infrared spectral range and fitted model.

The wavelength calibration curve can be used to roughly estimate the limits of the phase shaping capabilities of the pulse shaper. These considerations are based on the criterion that the pixel load $\delta\phi$ must not exceed π to avoid spectral distortions of the output pulse (compare section 2.2). Assuming for the moment a constant frequency spacing δf between the SLM pixels, the maximum group delay GD_{\max} that can be introduced using the pulse shaper is given by [25]

$$\text{GD}_{\max} = \frac{\delta\phi_{\max}}{2\pi\delta f} = \frac{1}{2\delta f}. \quad (4.1)$$

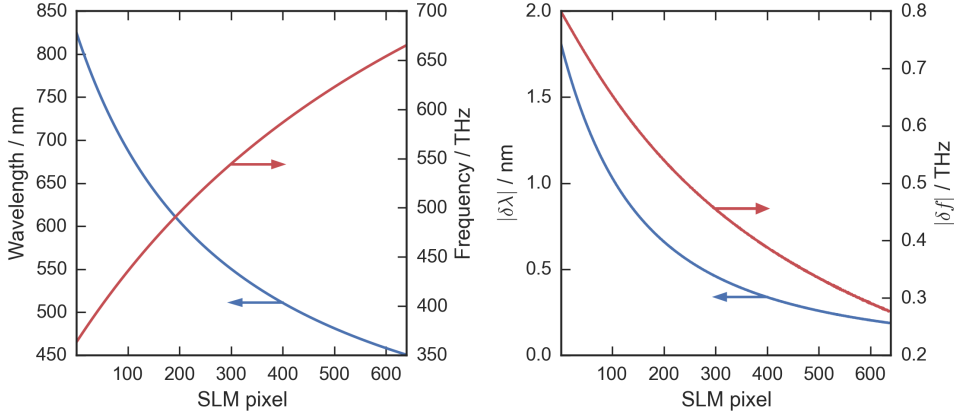


Figure 4.3.: *Left:* Pixel-to-wavelength and pixel-to-frequency mapping of the SLM. The curves were obtained by inverting the fitted model shown in figure 4.2. *Right:* Wavelength spacing $|\delta\lambda|$ and frequency spacing $|\delta f|$ between adjoining pixels as a function of pixel number.

Due to the non-linearity of the pixel-to-frequency mapping, the value of δf varies significantly over the working range of the pulse shaper. Thus the maximum group delay GD_{\max} was calculated separately for various centre wavelengths assuming that the frequency spacing δf is locally constant to a good approximation. The results are displayed in table 4.1. Since a group delay can be applied to a pulse both with positive and negative sign (corresponding to positive and negative shifts in time), the temporal window T in which accurate pulse shaping is possible is given by $T = 2\text{GD}_{\max}$ [34]. The values of T range from 1.4 ps to 2.3 ps which is similar to values reported in the literature for comparable pulse shaping setups [34, 61]. The temporal shaping window is of particular importance for pulse-shaper-based time-resolved spectroscopy experiments since it effectively limits the time scale on which dynamics can be investigated.

λ (nm)	$\delta\lambda$ (nm)	δf (THz)	GD_{\max} (fs)
750	1.3	0.7	700
650	0.8	0.6	850
550	0.4	0.4	1150

Table 4.1.: The upper limit for the group delay GD_{\max} as a function of centre wavelength.

Using similar considerations it is possible to estimate the maximum group delay dispersion (GDD) that can be applied to a pulse using the pulse shaper. In this case, the phase varies quadratically with frequency and the pixel load $\delta\phi$ increases linearly with the detuning from the pulse's centre frequency. The spectral width Δf of the pulse thus has to be taken into account. The maximum GDD can be estimated by requiring that the pixel load $\delta\phi$ must not exceed π at a detuning of $\Delta f/2$ from the centre frequency. This translates to [34]

$$\text{GDD}_{\max} = \frac{1}{2\delta f} \frac{1}{\pi\Delta f} = \frac{\text{GD}_{\max}}{\pi\Delta f}. \quad (4.2)$$

Table 4.2 shows GDD_{\max} as a function of spectral pulse width Δf for pulses centred at 550 nm and 750 nm. Notably, Δf should be determined at the base of the spectrum (e.g. at 10% of the maximum intensity) instead of using the FWHM. The results indicate that a substantial amount of material dispersion can be compensated for by the pulse

shaper. As an example, the value of $\text{GDD}_{\max} = 3050 \text{ fs}^2$ for a pulse at 550 nm with $\Delta f = 120 \text{ THz}$ is sufficient to compensate for roughly 40 mm of BK7 glass in the beam path. However, another effect which can lead to pulse distortions has not been included in these considerations. If the phase exceeds the maximum phase change that the LC pixels can introduce, the phase values need to be shifted by multiples of 2π . This results in voltage jumps between adjacent pixels, which, in turn, can lead to spectral distortions in the form of sharp dips or spikes.

Δf (THz)	GDD_{\max} (fs^2) at 550 nm	GDD_{\max} (fs^2) at 750 nm
80	4600	2800
100	3650	2200
120	3050	1850

Table 4.2.: Maximum group delay dispersion for various pulse widths Δf at 550 nm and at 750 nm.

Consequently, the results presented in table 4.2 represent a best-case scenario not taking non-ideal behaviour of the liquid crystal pixels into account, and pulse distortions are likely to occur already for values of the GDD lower than GDD_{\max} . Nonetheless, these considerations based on the wavelength calibration results provide a useful estimate of the dispersion compensation capabilities of the pulse shaping setup.

4.1.2. Phase calibration

A typical result from a phase calibration run is displayed in figure 4.4 which shows a plot of the voltage and wavelength dependent phase shift $\phi(U, \lambda)$ of LC mask *A* for wavelengths ranging from 684 nm to 814 nm. The phase is continuous and free of noise in both dimensions. Figure 4.4 also shows the voltage dependent phase at 700 nm and 800 nm. The curves have the characteristic shape that is common to all phase curves. At low voltages, the phase is practically constant, indicating that the voltage has not exceeded the threshold value ($\sim 80 \text{ mV}$) for rotating the elongated LC molecules. For voltages above threshold, the phase curve $\phi(U)$ can to a good approximation be described by a bi-exponential decay function with a dominant fast component. Typically the phase drops to about 10 % of its maximum value already around $U \sim 600 \text{ d.u.}$, corresponding to only 15 % of the voltage range of the SLM. At higher voltages the phase slowly approaches zero. For all practical purposes, only the phase above threshold is of interest, because the orientation of the LC molecules, and therefore the introduced phase shift, is not well defined for voltages below threshold.

The phase curves $\phi(U)$ at different wavelengths mainly differ in the maximum phase change which increases towards lower wavelengths. From independent phase calibration runs in the visible and near-infrared spectral range, the maximum phase was determined to be approximately 8π at 532 nm and 4.4π at 814 nm for a double pass through a single LC mask. This large working range has the advantage that phase patterns can be wrapped modulo a multiple of 2π , which leads to a lower number of voltage jumps and thus helps to avoid pulse distortions which are associated with a discontinuous driving voltage.

As described in section 3.2.3 of this report, the phase shift ϕ of an LC mask is calibrated by finding a function $\phi(U, \lambda)$ that reproduces the measured transmission $T(U, \lambda)$ of the pulse shaper according to $T(U, \lambda) = \cos^2 \phi(U, \lambda)$. The agreement between measured and reconstructed transmittance is thus an import criterion to asses the accuracy of the phase calibration. Figure 4.5 shows both the transmission reconstructed from the phase plotted

in figure 4.4 and the corresponding measured transmission. It is apparent that measured and reconstructed transmission are in perfect agreement, indicating that the retrieved phase accurately reflects the measured transmission behaviour of the pulse shaper.

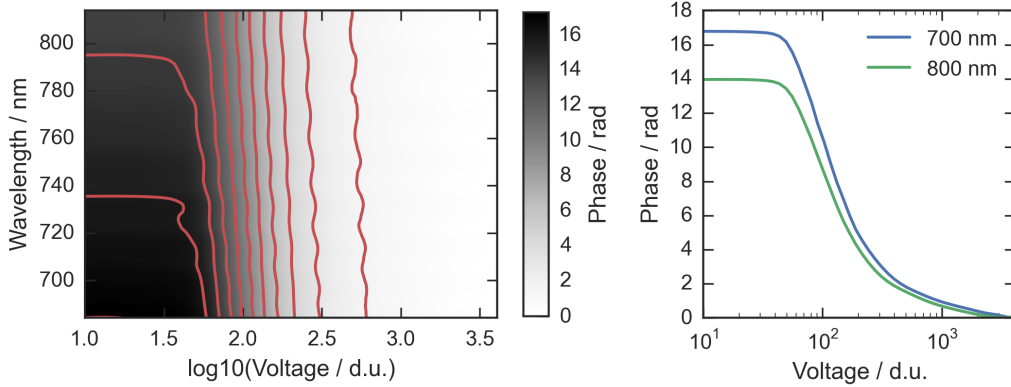


Figure 4.4.: *Left:* Phase $\phi(U, \lambda)$ introduced by the first LC mask of the LC-SLM as a function of wavelength and voltage. The contour lines are drawn at multiples of π . *Right:* Voltage dependant phase at 700 nm and 800 nm.

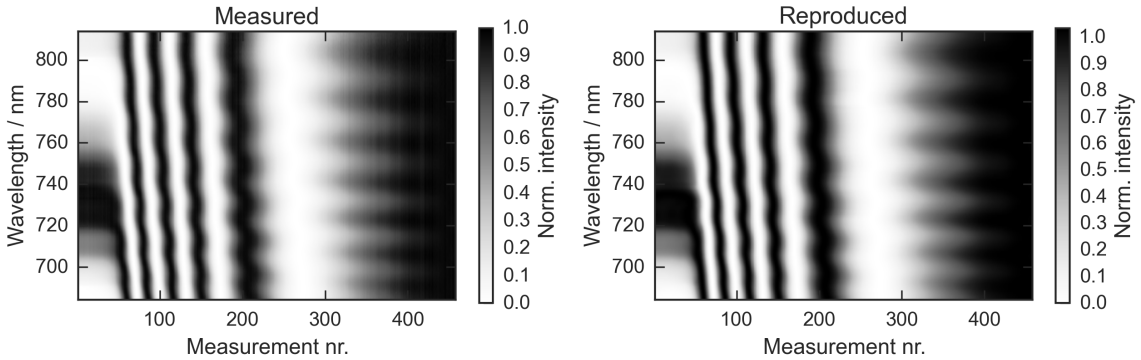


Figure 4.5.: *Left:* Measured transmitted intensity (normalised). *Right:* Intensity modulation of the pulse shaper calculated using the phase calibration results displayed in figure 4.4.

To compare the spline-based phase extraction algorithm used in this work to the conventional method based on direct inversion both approaches were used to retrieve the phase from an intensity trace that was distorted artificially by adding Gaussian noise with a standard deviation corresponding to 5% of the maximum intensity. The resulting phase curves are shown in figure 4.6. The phase curve obtained from direct inversion is clearly affected by the noise which causes distinct aberrations at the positions of intensity extrema (see inset in figure 4.6). The method developed in this work, on the other hand, produces a smooth phase curve despite the presence of noise. To further compare the robustness of the two methods, they were used to retrieve the phase from intensity traces with a varying amount of noise added. To characterise the resulting phase curves, the root-mean-square-deviation (RMSD) with respect to a reference phase curve was determined for multiple values of the standard deviation of the (Gaussian) noise. The results, i.e., the RMSD as a function of noise level, are shown in figure 4.7. For both methods, the RMSD generally increases with the noise level. However, at all noise levels the phase curves retrieved via spline optimisation deviate less from the reference phase than the results from direct phase retrieval, with RMSD values differing by a factor of 3 to 4. As

a conclusion, these findings show that the spline-based method for phase retrieval developed in the frame of this work is superior to the standard method with respect to noise susceptibility.

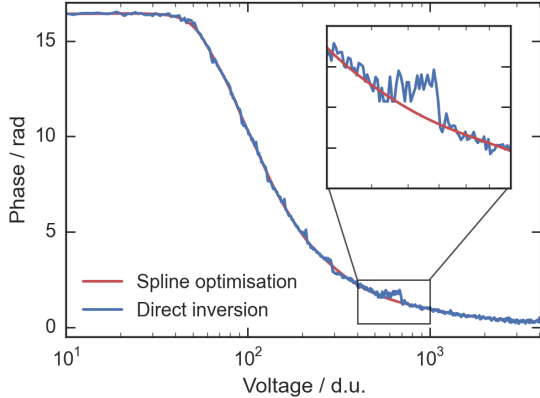


Figure 4.6.: Phase calibration curves retrieved by direct inversion (blue) and via spline optimisation (red).

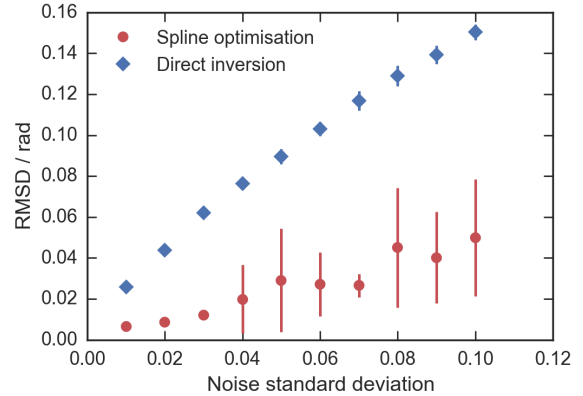


Figure 4.7.: RMSD as a function of noise standard deviation. The values have been obtained by averaging over 25 independent phase retrieval runs. The error bars correspond to one standard deviation.

In addition to the voltage dependent intensity modulation, the phase calibration spectrograms also show an oscillatory modulation of the spectral intensity at certain driving voltages. These modulations are visible as horizontal stripes in the normalised spectrogram displayed in figure 4.5, and they are reproduced by the phase calibration procedure (see figure 4.5, right panel). Notably, the relative amplitude of these sinusoidal modulations varies significantly with the driving voltage, whereas the modulation frequency remains practically constant. The modulation is particularly pronounced if the overall transmitted intensity is low, whilst hardly any modulations are visible at high intensities. This is illustrated in figure 4.8 which shows vertical cuts of the phase calibration spectrogram before normalisation at different voltage values. Fourier transforms of the modulated spectra show that the oscillation period of the spectral modulations is approximately 10 THz. In the time domain, this corresponds to an attenuated replica pulse with a delay of 100 fs with respect to the main pulse.

These periodic modulations presumably originate in the multilayer structure of the LC-SLM which is shown in figure 3.2. In each LC mask, the thin liquid crystal layer is sandwiched between two ITO electrodes which exhibit a large refractive index ($n = 1.87$ at 633 nm) as compared to the liquid crystal ($n_o = 1.51$ at 633 nm). This refractive index discontinuity causes a small fraction of the traversing light to be reflected at the boundary between liquid crystal and ITO. As a result, the LC layer framed by the ITO electrodes acts as a low-finesse Fabry-Perot interferometer resulting in a periodically varying transmittance. This effect is known to occur in LC displays [62]. This hypothesis is supported by the fact that refractive index and thickness of the LC layer (10 μm) give rise to a free spectral range¹ of about 10 THz for this multilayer structure which matches the observed oscillation period of the spectral modulations.

On the other hand, the relative amplitude of the intensity modulation resulting from

¹The free spectral range $\Delta\nu = c/2nd$ is the frequency spacing between adjoining transmittance maxima. c is the speed of light, n the refractive index and d the thickness of the LC layer.

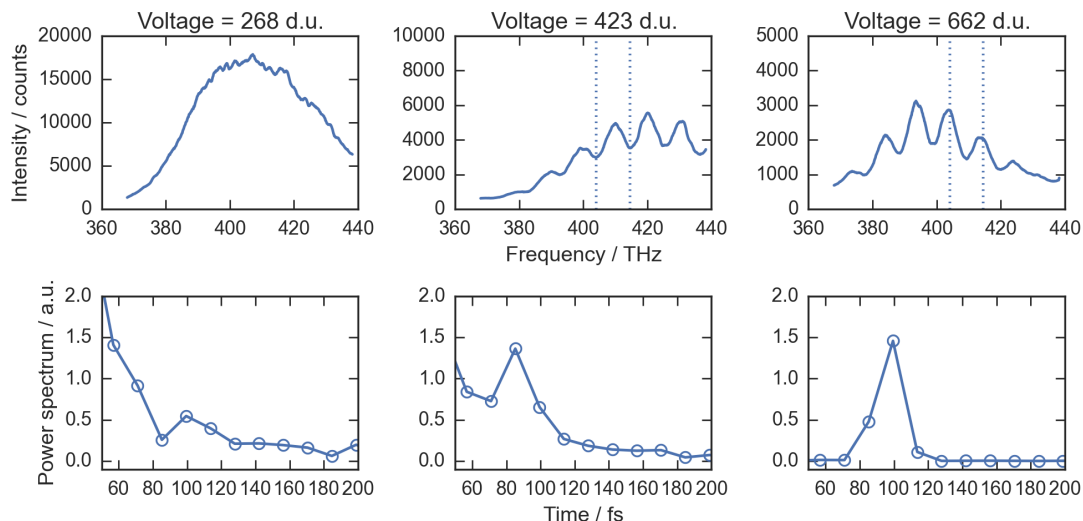


Figure 4.8.: Vertical cuts of the phase calibration spectrogram (before normalisation) at three different voltages. After transmission through the pulse shaper, the laser spectrum is periodically modulated. The relative amplitude of the modulations is voltage dependent whereas the frequency is practically constant (~ 10 THz). Power spectra of the spectral amplitudes are shown in the bottom panels.

a simple Fabry-Perot effect should be independent of the maximum intensity. This is in contradiction to the observations which show that the relative amplitude of the modulation depends on the applied driving voltage. However, one has to take into account that the LC-SLM has a more complex structure than a simple Fabry-Perot interferometer. In particular, the effect of the voltage dependent birefringence of the LC layers has to be taken into account, and it is shown in reference [63] that this can indeed lead to a voltage dependent amplitude of the Fabry-Perot interferences.

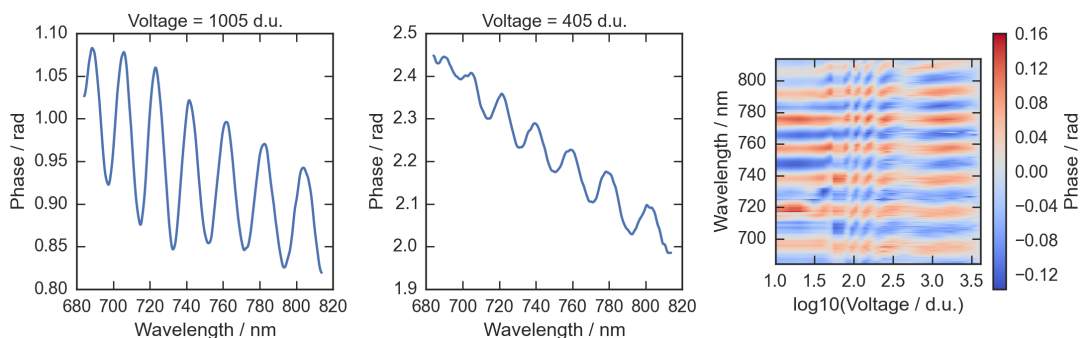


Figure 4.9.: *Left and centre:* Wavelength dependent phase at driving voltages 1005 d.u. and 405 d.u.. The phase features distinct oscillations with a peak-to-peak value of the order of 0.1 rad to 0.2 rad. *Right:* Oscillatory component of the phase plotted in figure 4.4.

Since the spectral modulations are reproduced by the phase calibration procedure (see figure 4.4), the phase $\phi(U, \lambda)$ is also periodically modulated. This is illustrated in figure 4.9 where plots of the wavelength dependent phase of LC mask *A* at two different voltages are shown. The curves feature clear oscillations with a peak-to-peak value of the order of 0.1 rad to 0.2 rad. Figure 4.9 also shows a heatmap plot of the oscillatory component of the phase shown in figure 4.9. It is evident that the oscillatory modulation is present over the whole voltage range without a substantial variation in frequency or amplitude.

Only for voltages within a small number of narrow voltage-bands does the modulation amplitude appear to be attenuated (visible as vertical stripes in figure 4.9). The question as to which extent this modulation affects the pulse shaping accuracy was investigated in the context of amplitude shaping experiments (see section 4.2).

4.2. Amplitude shaping

Results from wavelength and phase calibration runs suggest that the pixel-to-wavelength mapping as well as the wavelength and voltage dependent phase shift of the LC masks could be accurately determined. Ultimately, however, the accuracy of calibration procedure needs to be gauged on the basis of pulse shaping experiments where the calibration results are put to the test. To this end, amplitude shaping experiments were performed where the calibration results were used to specifically manipulate the spectral intensity of near-infrared laser pulses.

In a first experiment, transfer functions describing a periodic modulation of the spectral amplitude were applied to the laser pulses via the pulse shaper. The appropriate voltage patterns were derived following the scheme described in section 3.2.4. Three exemplary results are presented in figure 4.10: Amplitude modulation according to $A = \cos^2(2\pi\lambda/\lambda_0)$ with $\lambda_0 = 40$ nm (*top panel*) and $\lambda_0 = 20$ nm (*centre panel*) and binary amplitude shaping resulting in regularly spaced spectral holes with a width of 15 nm (*bottom panel*). In each plot, the laser spectrum before shaping is shown as a blue curve and the desired spectral shape is indicated by a dashed red line. In all three cases, the shaped spectrum is in very good agreement with the target shape. For the \cos^2 -like amplitude modulation aberrations mainly occur at the intensity maxima where the shaped spectrum in some cases fails to reach the target intensity. This effect is more pronounced for smaller modulation periods as shown in the centre panel of figure 4.10. For even higher modulation frequencies, the shaping accuracy further deteriorates, in particular with respect to the achievable modulation depth. Presumably, this is because fast spectral modulations require a large pixel load, which, in turn, leads to spectral distortions due to destructive interference between neighbouring pixels (see section 2.2). However, the results shown in figure 4.10 indicate that spectral features with a FWHM down to about 4 nm can be shaped with reasonable accuracy.

In the case of binary amplitude shaping, deviations from the ideal shape can be seen at the edges of the spectral holes where the abrupt change from extinction to full transmittance occurs. This transition is smoothed out to some extent due to finite spectral resolution of the pulse shaper. This is illustrated in the inset in figure 4.10.

It was found during the analysis of the calibration results that the calibrated phase $\phi(U, \lambda)$ exhibits distinct oscillations as a function of wavelength. These periodic modulations presumably originate from a Fabry-Perot effect inside the LC-SLM. To investigate to which extent these oscillations affect the pulse shaping accuracy, the oscillatory component was removed from the phase, and the resulting, modulation-free set of phase calibration functions (one for each LC mask) was compared to the original calibration data with respect to amplitude shaping accuracy. To remove the oscillating component, a 3rd-order polynomial was fitted to the wavelength dependent phase at each voltage. The polynomial fit captures the slowly varying component of the phase but the fast oscillations are effectively averaged out. Both calibration sets were used to modulate the spectral amplitude of laser pulses according to $A = \cos^2(2\pi\lambda/100 \text{ nm})$. The results are presented in figure 4.11. In both cases, the measured spectral intensity is in good agreement with

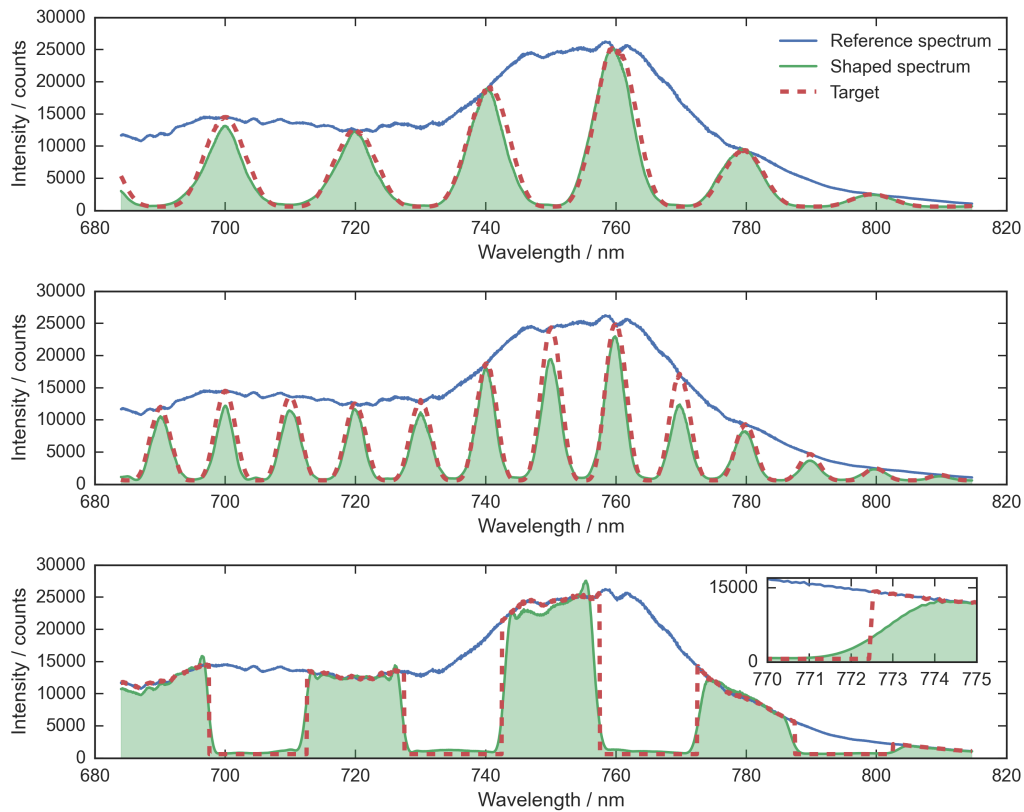


Figure 4.10.: Results of amplitude shaping experiments. The blue curve represents the (unshaped) reference spectrum, the green, shaded curve is the measured spectrum after shaping and the red, dashed line indicates the desired spectral shape. *Top:* Periodic amplitude modulation with neighbouring peaks separated by 20 nm. *Centre:* Periodic amplitude modulation with neighbouring peaks separated by 10 nm. *Bottom:* Binary amplitude modulation resulting in spectral holes with 15 nm width.

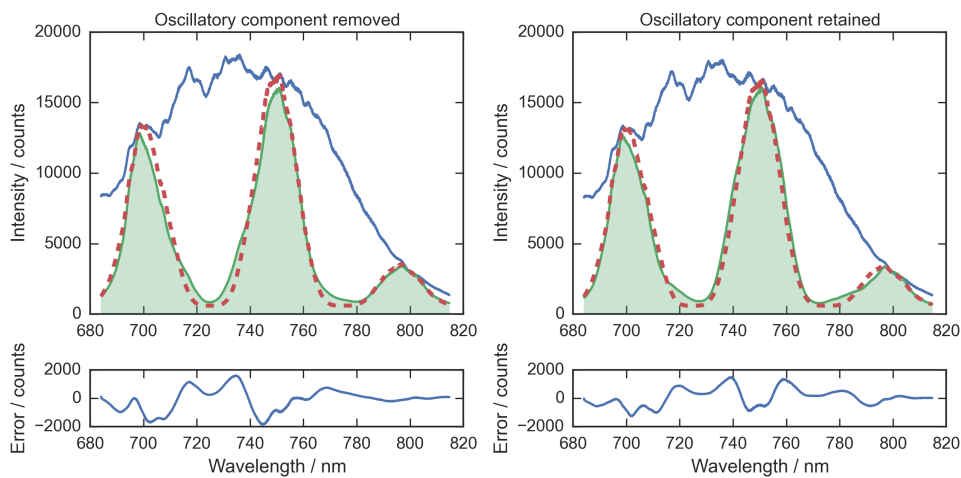


Figure 4.11.: *Left:* Amplitude shaping with the oscillatory component of the phase removed. *Right:* Amplitude shaping with the oscillatory component of the phase retained. In the bottom panels, the deviation between measured and desired spectral shape is plotted.

the target shape, which is indicated by the dashed red line. Calculations show that in this case the root-mean-square-deviation between desired and measured spectral shape is slightly smaller if the oscillatory features of the phase are retained. However, for a different transfer functions the situation is reversed, i.e., slightly better results are obtained with the oscillatory features removed. This suggests that the periodic modulation of the phase does not systematically affect the pulse shaping accuracy, and that deviations from the desired pulse shape are more likely to originate directly in interference effects in the LC-SLM.

To demonstrate that the amplitude shaping capabilities of the pulse shaper go beyond periodic intensity modulation, the device was used to reproduce arbitrary greyscale images. To this end, the greyscale values of each line of a reference picture were translated to a transfer function with maximum greyscale values corresponding to full and minimum greyscale values corresponding to zero transmittance, respectively. Subsequently, the transfer function was applied to the laser pulses via the pulse shaper and the resulting spectral intensity was recorded. By repeating this procedure for every pixel row of the reference image, a replica image was constructed line by line which each row given by the greyscale-coded spectral intensity of the shaped laser pulse.

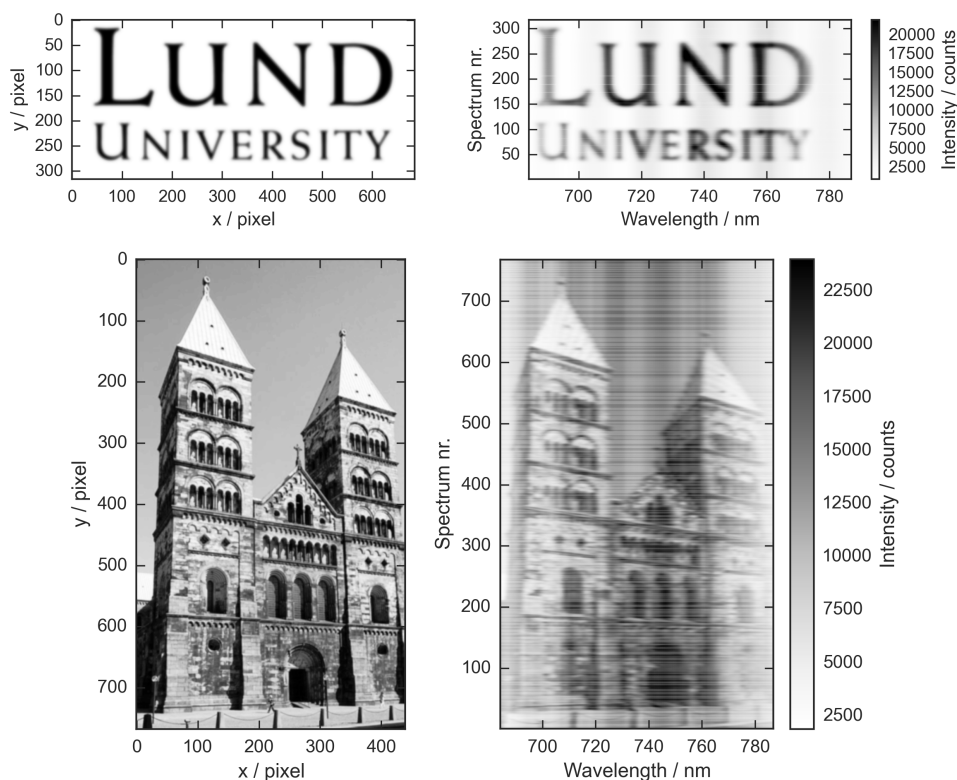


Figure 4.12.: Line by line reproduction of greyscale images using the amplitude shaping capabilities of the pulse shaper. Reference images are shown on the left hand side. The image of the Lund cathedral was derived from a photo by Anton Holmquist and Pauline Gyllengahm licensed under the Creative Commons (CC BY 4.0) license. Each line of the reproduced images (right hand side) is given by the colour-coded spectral intensity of a shaped laser pulse.

Two reference images - a binary image showing the Lund university logo and a greyscale image of the Lund cathedral - and the corresponding replicas are displayed in figure 4.12. For image reconstruction, the spectral intensity in the range from 680 nm to 790 nm was modulated, corresponding to 90 SLM pixels. The central features of the reference

images could be accurately reproduced by the pulse shaper. In particular, the various shading levels characterising the image of the Lund cathedral are for the most part clearly distinguishable in the reconstructed image. However, fine details cannot be reproduced in the replica image and the contrast level of the reference images cannot be reached. These limitations arise inherently as a consequence of the limited number of pixels which were available for shaping and the finite spectral resolution of the pulse shaper.

4.3. Pulse compression

A special feature of the pulse shaping setup used in this work is the use of a highly-dispersive prism to spatially separate the spectral components of the input pulses. As a consequence, substantial amounts of material dispersion are introduced by the pulse shaper itself, leading to severe temporal broadening of the output pulses. To verify the phase shaping capabilities of the pulse shaper, it was used to re-compress the output laser pulses by compensating for the non-linear phase introduced by the prism and the glass windows of the LC-SLM.

As a first experiment, the pulse shaper alone was employed to re-compress the output pulses without the use of an additional prism compressor. The input pulses used in this experiment had a temporal duration of 18.7 fs (assuming Gaussian shape) with a spectrum centred around 750 nm as shown in figure 4.13. The pedestal width of the spectral intensity (taken at 10 % of the maximum value) is 172 nm or 92 THz. The appropriate phase patterns for recompression were derived by calculating the full phase χ introduced by the prisms and the SLM windows, followed by an extraction of the 2nd and 3rd order phase contributions via a polynomial fit. Subsequently, the 2nd and 3rd order phase was inverted and mapped to the LC-SLM. The full phase χ as a function of optical frequency ν is given by

$$\chi(\nu) = \frac{2\pi\nu n_P}{c_0} d_P + \frac{2\pi\nu n_W}{c_0} d_W. \quad (4.3)$$

$n_{P/W}$ denotes the (wavelength dependent) refractive index of the prism (P) or the SLM windows (W), respectively. The refractive index of the prism material (N-SF11) is given in reference [53]. The material of the windows is not specified in the SLM manual, and it was thus assumed that they consist of fused silica which is commonly used in optical components (The refractive of fused silica is given in reference [64]). The total thickness of the glass windows is specified as 6 mm by the manufacturer, resulting in $d_W = 12$ mm for a double pass. However, the path length d_P in the prism was not known a priori. The best phase configuration was therefore determined by monitoring the degree of recompression while systematically varying the value of d_P entering the phase calculation according to equ. 4.3. The re-compression was characterised by the intensity autocorrelation signal at zero delay. Results are presented in figure 4.14 which shows a plot of the autocorrelation signal strength as a function of compensated material thickness d_P . The highest signal strength, indicating the shortest pulse duration, is reached if the pulse shaper is programmed to compensate for 7.5 mm of SF-11 glass and 12 mm of fused silica. At 750 nm, this corresponds to a GDD of 2040 fs² that is compensated for.

Full autocorrelation traces for three different dispersion compensation configurations (6 mm, 7.5 mm and 9 mm of SF-11) are shown in figure 4.15. The plots clearly show that the temporal width of the output pulse is affected by the applied phase pattern. For the optimum compensation setting found before ($d_P = 7.5$ mm) the autocorrelation

peak has a temporal width of 37.4 fs, which corresponds to a pulse duration of about 26.4 fs, assuming a Gaussian pulse shape. This value is considerably larger than the duration of the input pulses (18.7 fs), which shows that complete recompression could not be achieved with the pulse shaper alone. This can be attributed to two effects. First, a comparison with the pulse shaper limits derived from the wavelength calibration (see table 4.2) shows that the compensation of 2040 fs^2 of GDD plus 1300 fs^3 of third order phase will lead to pixel loads close to π at the edge of the spectrum (for 90 THz spectral width). Consequently, spectral narrowing occurs, resulting in an increased pulse duration. Second, during these experiments, an early version of the *LabVIEW* code for the generation of voltage patterns was used that did not exploit the full phase range of the pulse shaper. As a result, a relatively high number of voltage jumps occurred, possibly leading to a degradation of the spectrum at the position of the jumps. By using the full phase range, the number of voltage jumps can be reduced considerably (illustrated in figure 4.16), and it is expected that this will result in an improved re-compression efficiency. However, due to time constraints, these experiments could not be repeated with an updated version of the *LabVIEW* code.

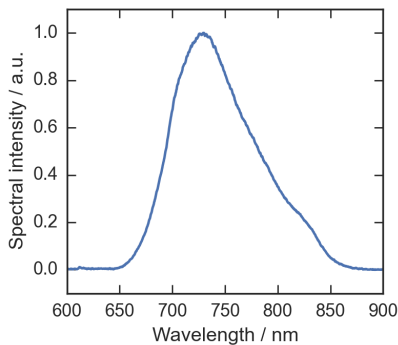


Figure 4.13.: Spectrum of the input pulses at the NOPA output.

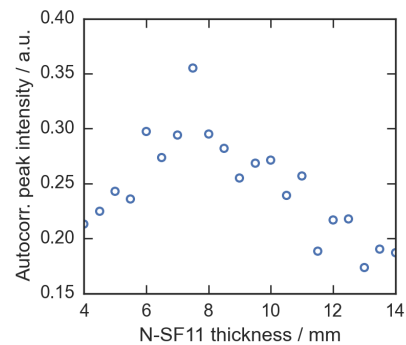


Figure 4.14.: Autocorrelation signal at zero delay as a function of compensated material thickness.

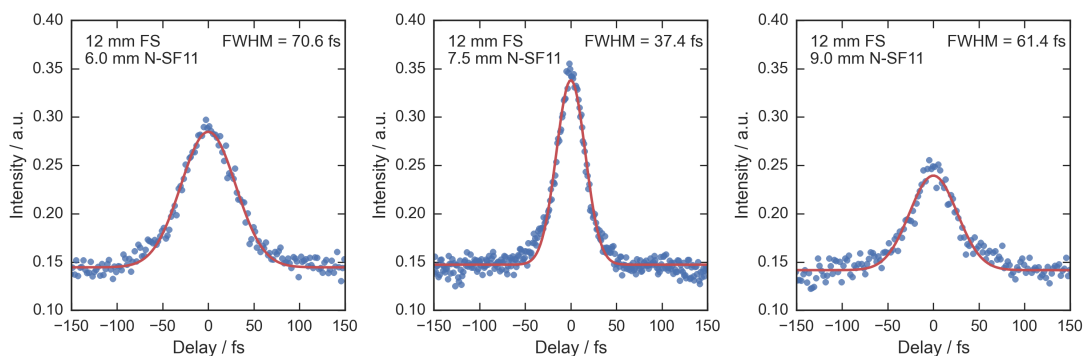


Figure 4.15.: Intensity autocorrelation traces measured with three different dispersion compensation settings. The FWHM given in the subplots refers to the autocorrelation trace. The pulse width can be obtained from this value by multiplication with $1/\sqrt{2}$ (assuming a Gaussian pulse shape).

In an additional experiment, a prism compressor consisting of two fused silica prisms at a separation of 128 cm in double pass configuration was used to partially compensate

for the material dispersion in the pulse shaping setup. This substantially reduced the amount of material dispersion that needed to be compensated for by the pulse shaper itself, leading to an overall decrease in the pixel load and the number of phase jumps. To find the phase settings leading to the optimum pulse compression with this setup, the expansion coefficients of the phase applied with the pulse shaper were optimised manually with regard to the autocorrelation signal at zero delay. The phase was expressed in terms of a Taylor expansion up to fourth order around 740 nm. With the optimum phase pattern found in this way, output pulse durations of 16.5 fs could be achieved. This value is slightly below the input pulse duration (18.7 fs) and considerably smaller than the shortest pulse duration that was achieved without an additional prism compressor (26.4 fs). The expansion coefficients of the optimum phase pattern are presented in table 4.3. As compared to the previous case without external precompression, the GDD that needs to be compensated for by the pulse shaper is reduced by more than 50 % (900 fs² vs. 2040 fs²), which underlines the significance of the prism compressor. Furthermore, for a GDD of 900 fs² the pixel load should remain well below π across the whole pulse spectrum, meaning that spectral degradation due to pixelation effects is not expected to occur.

ϕ_2	ϕ_3	ϕ_4
-900 fs ²	-600 fs ³	-2000 fs ⁴

Table 4.3.: Taylor coefficients of the phase resulting in the minimum output pulse duration. The phase was expanded around 405 THz (740 nm).

Autocorrelation traces of the input and the compressed output pulse are shown in figure 4.17. As shown in subplot (c) of this figure, the main difference between the autocorrelation traces of the input and output pulse is that the former exhibits more distinct wings. These wings typically occur as a consequence of third order phase distortions, and the fact that these wings are less pronounced after recompression suggests that 3rd order phase contributions present in the input pulse could be removed with the pulse shaper.

However, even though the pulses could be recompressed successfully, room for improvement remains: Fourier transforming the spectral amplitude of the input pulses shows that the input pulse spectrum shown in figure 4.13 can support bandwidth-limited pulses with duration of about 10 fs which is clearly lower than the shortest pulse duration that was achieved. These findings suggest that the spectral phase of the pulses exhibits complex features that cannot be described in terms of a (low order) Taylor expansion. Instead, a more flexible representation of the phase would be required to achieve compression down to the bandwidth limit. One possible approach would be to describe the phase in terms of spline whose control points are optimised in a closed-loop-scheme using the autocorrelation signal as feedback. A similar approach has been successfully applied in reference [65] to demonstrate pulse compression from 100 fs to 35 fs. Alternatively, an open-loop-scheme can be employed for pulse compression as demonstrated in [34] where a prism-based pulse shaper was used in combination with a SPIDER setup for complete pulse characterisation to compensate for substantial amounts of material dispersion without any iteration.

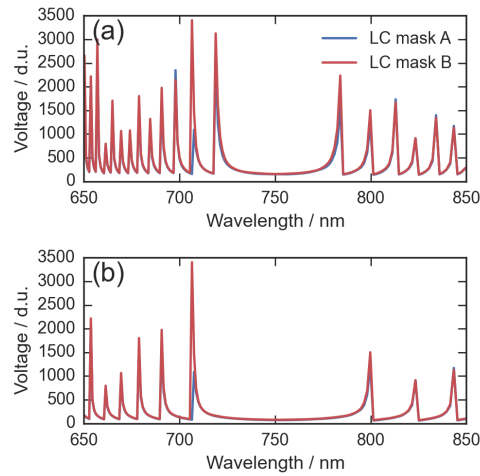


Figure 4.16.: Voltage patterns required to compensate for the material dispersion of 7.5 mm SF-11 and 12 mm fused silica. In (a), phase values are constrained to the interval $[0, 2\pi]$, whereas the working range in (b) is 4π , leading to reduced number of phase (and voltage) jumps.

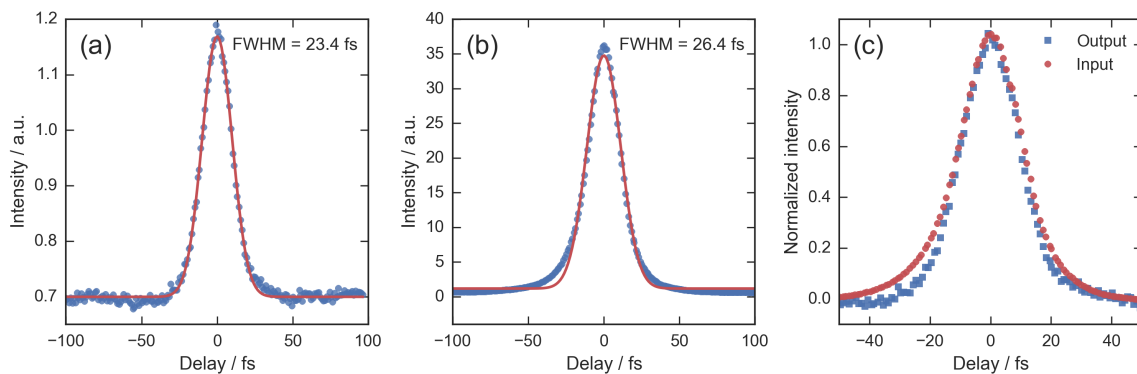


Figure 4.17.: Results of pulse recompression using the pulse shaper plus an additional prism compressor. (a) Intensity autocorrelation trace of the output pulse and Gaussian fit. (b) Intensity autocorrelation trace of the input pulse and Gaussian fit. (c) Plot of both autocorrelation traces for comparison.

5. Summary and Outlook

A programmable Fourier-transform pulse shaper for phase and amplitude shaping of femtosecond laser pulses was implemented in the frame of this project. The device is intended for dispersion compensation and pulse sequence generation for ultrafast spectroscopy experiments. Pulse-shaper-assisted two-dimensional coherent nanoscopy experiments, in particular, are expected to give new insights into coherent phenomena in nanostructures on the femtosecond time scale.

The pulse shaper is based on a liquid crystal spatial light modulator (LC-SLM) which needs to be calibrated carefully in order to achieve accurate pulse shaping. Routines for determining the pixel-to-wavelength mapping and the wavelength dependent voltage-to-phase mapping of the LC-SLM have been implemented. Amplitude shaping experiments were performed to assess the accuracy of the calibration results. Within the limitations of the pulse shaper, very good agreement between measured and desired spectral shapes was found, and it is concluded that the pulse shaper could be successfully calibrated using the methods presented in this work.

The phase calibration procedure introduced in this report determines the voltage-to-phase mapping indirectly from an *in situ* measurement of the intensity modulation behaviour of the pulse shaper. The phase is retrieved using an iterative optimisation procedure which was found to be superior to the conventional method for phase extraction with regard to noise susceptibility. In particular, the appearance of non-physical jumps in the phase curves due to aberrations in the calibration data could be successfully suppressed. Estimates for the limitations of the pulse shaper were derived from the wavelength calibration results. It was found that the available spectral resolution leads to a temporal shaping window at the order of 1 ps to 2 ps, depending on the spectral region. This determines the timescale which can be investigated in ultrafast spectroscopy experiments relying solely on the pulse shaper for laser pulse sequence generation.

Both amplitude shaping experiments and phase calibration runs revealed that a periodic modulation is superimposed on the spectra of the output pulses. The amplitude of these modulations is at the order of a few percent of the input intensity and their oscillation frequency suggests that they originate in a Fabry-Perot effect caused by the multilayer structure of the SLM. This implies that the effect is unavoidable.

The phase control capabilities of the pulse shaper were demonstrated by compensating for material dispersion introduced by the dispersing prism in the setup. With the pulse shaper alone, complete recompression could not be achieved because spectral narrowing occurred as a consequence of high pixel loads. With external precompression by means of a prism compressor, on the other hand, the material dispersion could be compensated for successfully. These findings clearly show that additional compression is necessary if the pulse shaper is employed for shaping of broadband laser pulses.

Even though successful recompression of the output pulses could be demonstrated, bandwidth-limited pulse durations could not be achieved. Presumably, this is because the full phase range of the LC-SLM was not exploited and due to the simplicity of the recompression procedure. A logical next step would thus be to develop an improved pulse

compression scheme that makes use of the full potential of the pulse shaper and is capable of compensating for arbitrary spectral phase distortions. A possible approach would be to optimise the applied phase pattern by means of an evolutionary algorithm. Considering the flexibility of the pulse shaper, it is expected that nearly bandwidth limited pulses can be achieved in this way.

Following pulse compression, a next step toward 2D nanoscopy should be to demonstrate the generation of pulse sequences with control over inter-pulse delay and relative phases. Special attention should be given to the accuracy of the temporal pulse spacing, since this is of paramount importance for obtaining clear 2D spectra.

With these steps taken, the pulse shaper will be available for dispersion control and pulse sequence generation for ultrafast spectroscopy and nanoscopy experiments.

A. Appendix

A.1. Spectral phase expansion coefficients

The additional spectral phase accumulated by a laser pulse after propagation through material with refractive index n and thickness d is given by:

$$\psi(\omega) = k(\omega)d = \frac{\omega n(\omega)L}{c} \quad (\text{A.1})$$

Commonly, the phase is expanded as a Taylor series around the centre frequency ω_0 of the pulse according to $\psi = \sum_n \psi_n(\omega - \omega_0)^n/n!$. The coefficients ψ_i up to third order are given by:

$$\begin{aligned} \psi_0 &= \frac{n\omega_0 L}{c} \\ \psi_1 &= \frac{nL}{c} + \frac{\omega_0 d}{c} \frac{dn}{d\omega} \\ \psi_2 &= \frac{2L}{c} \frac{dn}{d\omega} + \frac{\omega_0 L}{c} \frac{d^2 n}{d\omega^2} \\ \psi_3 &= \frac{3L}{c} \frac{d^2 n}{d\omega^2} + \frac{\omega_0 L}{c} \frac{d^3 n}{d\omega^3} \end{aligned} \quad (\text{A.2})$$

The refractive index and its derivatives are evaluated at the centre frequency ω_0 . Often, expressions for the coefficients in terms of the centre wavelength λ_0 are useful. These can be derived directly from the above equations taking into account that

$$\lambda = \frac{2\pi c}{\omega} \quad \text{and} \quad \frac{d}{d\omega} = -\frac{\lambda^2}{2\pi c} \frac{d}{d\lambda}. \quad (\text{A.3})$$

The resulting expressions for the coefficients ψ_i are listed below. Again, the refractive index and its derivatives are taken at the centre wavelength λ_0 .

$$\begin{aligned} \psi_0 &= \frac{2\pi nL}{\lambda_0} \\ \psi_1 &= \frac{nL}{c} - \frac{\lambda_0 L}{c} \frac{dn}{d\lambda} \\ \psi_2 &= \frac{\lambda^3 L}{2\pi c^2} \frac{d^2 n}{d\lambda^2} \\ \psi_3 &= -\frac{\lambda^4 L}{4\pi^2 c^3} \left[3 \frac{d^2 n}{d\lambda^2} + \lambda \frac{d^3 n}{d\lambda^3} \right] \end{aligned} \quad (\text{A.4})$$

A.2. Pulse shaper transfer function

In this section, the derivation of the transfer function of the double liquid crystal mask in combination with entrance and exit polariser will be demonstrated. The derivation is based on the Jones formalism, which is used to describe polarised light and the effect of polarisation optics. An introduction to the formalism is given in reference [45]. We consider now a monochromatic wave polarised in x -direction propagating along z through a single pixel of the double mask. The situation is illustrated in figure A.1. The Jones vector representation of the optical wave is given by

$$\mathbf{E}_{\text{in}} = \begin{pmatrix} E_0 \\ 0 \end{pmatrix} e^{i(\omega t - kz)}. \quad (\text{A.5})$$

The effect of the whole assembly - polarisers plus LC pixels - on the light wave can be described in terms of the Jones matrix J_{tot} of the arrangement. More precisely, the output field is given by $\mathbf{E}_{\text{out}} = J_{\text{tot}} \mathbf{E}_{\text{in}}$. The matrix J_{tot} given by the product of the Jones matrices of the individual components in the setup:

$$J_{\text{tot}} = J_P J_B J_A J_P \quad (\text{A.6})$$

Here, J_P is the Jones matrix of the polarisers and J_A and J_B denote the Jones matrices of the first (active axis at -45°) and second (active axis at $+45^\circ$) LC pixel, respectively. J_P is simply given by

$$J_P = \begin{pmatrix} 1 & 0 \\ 0 & 0 \end{pmatrix} \quad (\text{A.7})$$

The Jones matrix of the first LC pixels reads:

$$J_A = R(-\pi/4) \begin{pmatrix} 1 & 0 \\ 0 & e^{-i\Delta\phi_1} \end{pmatrix} R(\pi/4) \quad \text{with} \quad R(\theta) = \begin{pmatrix} \cos \theta & \sin \theta \\ -\sin \theta & \cos \theta \end{pmatrix} \quad (\text{A.8})$$

Analogously, the Jones matrix of the second LC pixel with its active axis at $+45^\circ$ is given by

$$J_B = R(\pi/4) \begin{pmatrix} 1 & 0 \\ 0 & e^{-i\Delta\phi_2} \end{pmatrix} R(-\pi/4). \quad (\text{A.9})$$

The Jones matrices of the LC pixels are given by the Jones matrix of a wave retarder introducing a phase delay $\Delta\phi_{A/B}$. However, since the active axes are rotated by $\pm 45^\circ$, a coordinate transformation is applied to obtain the corresponding Jones matrices in the reference coordinate system (indicated in figure A.1). Compiling the above results gives the Jones matrix of the complete assembly:

$$J_{\text{tot}} = \frac{1}{2} \begin{pmatrix} e^{-i\Delta\phi_A} + e^{-i\Delta\phi_B} & 0 \\ 0 & 0 \end{pmatrix} \quad (\text{A.10})$$

Applying this transfer matrix to the input field gives the following output:

$$\mathbf{E}_{\text{out}} = \cos \left(\frac{\Delta\phi_A - \Delta\phi_B}{2} \right) \exp \left(-i \frac{\Delta\phi_A + \Delta\phi_B}{2} \right) \mathbf{E}_{\text{in}} \quad (\text{A.11})$$

The key points are that the amplitude is modulated according to $\cos \left(\frac{\Delta\phi_A - \Delta\phi_B}{2} \right)$ and that

a phase retardation $\frac{\Delta\phi_A + \Delta\phi_B}{2}$ has been introduced, i.e. equation A.11 describes an output field that has been shaped with respect to phase and amplitude. Notably, the amplitude modulation is governed by the sum of the phase shifts $\phi_{A/B}$ while the introduced spectral phase is determined by their sum. This enables independent phase and amplitude shaping.

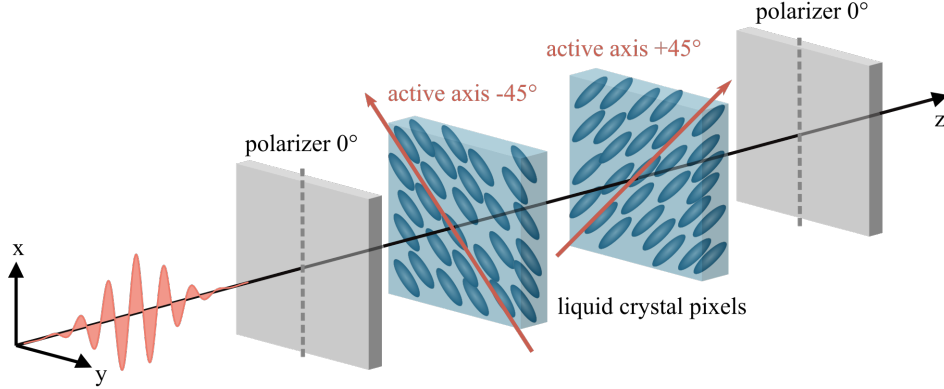


Figure A.1.: Schematic drawing of a setup for phase and amplitude shaping with liquid crystal modulators. The assembly consists of an entrance polariser, two pixelated liquid crystal masks (only a single pixel shown here) and an exit polariser. The active axis (see main text) of the masks are at $\pm 45^\circ$ with respect to the x -axis.

A.3. Pulse shaper dispersion law

The dispersion law $p(\lambda)$ of the pulse shaper, i.e. the lateral displacement of the spectral components at the LC-SLM, can be derived from the dispersion law of a prism and simple geometrical considerations.

The pulse shaper dispersion law is based on the law describing ray deflection by a prism. A ray incident at an angle θ_i is deflected by an angle θ_d given by

$$\theta_d(\lambda) = \theta_i - \alpha + \arcsin \left[\sqrt{n(\lambda)^2 - \sin^2(\theta_i)} \sin(\alpha) - \sin(\theta_i) \cos(\alpha) \right]. \quad (\text{A.12})$$

The situation is shown schematically in figure A.2. α is the apex angle of the prism and $n(\lambda)$ is the wavelength dependent refractive index of the prism material. Equation A.12 can be derived by applying Snell's law twice, once at each boundary. In the pulse shaping setup, the ingoing beam is dispersed by the prism and the spectral components propagate in diverging directions until they are re-collimated by the focusing mirror, after which they propagate in parallel fashion. The lateral displacement $d(\lambda)$ of a spectral component with respect to the center line of the setup is therefore the same at the focusing mirror and at the SLM. The displacement $d(\lambda)$ is given by $d = f \tan \delta(\lambda)$ (see figure A.3) with the focal length f . δ is the angle that a deflected spectral components makes with the z -axis. It is related to the angle of incidence θ_i at the prism and the deflection angle θ_d via

$$\delta = \theta_d - \theta_i + \alpha + \beta - \frac{\pi}{2}. \quad (\text{A.13})$$

The situation is illustrated in figure A.3. The angle β describes the orientation of the prism. By inserting the expression for θ_d given in equation A.12 one arrives at the following

expression for the angle δ :

$$\delta(\lambda) = \beta - \frac{\pi}{2} + \arcsin \left[\sqrt{n(\lambda)^2 - \sin^2(\theta_i)} \sin(\alpha) - \sin(\theta_i) \cos(\alpha) \right] \quad (\text{A.14})$$

The position $p(\lambda)$ of a single spectral components in units of pixels at the SLM can then be expressed as

$$p(\lambda) = p_0 + \eta f \tan [\delta(\lambda)] \quad (\text{A.15})$$

Here, f is the focal length, $\eta = 10/\text{mm}$ is the density of pixels and p_0 the pixel hit by the spectral component that propagates in z -direction ($\delta = 0$) directly after the prism. For simplicity, it was assumed that the SLM was perfectly centered, i.e. $p_0 = 320$.

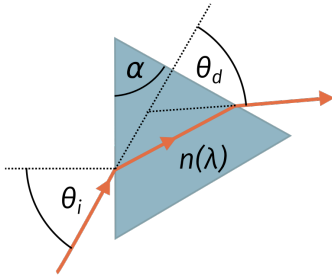


Figure A.2.: Deflection of a ray by a prism. θ_i is the angle of incidence, θ_d denotes the angle of deflection. The wavelength dependent refractive index of the prism material is denoted $n(\lambda)$ and α is the apex angle. The refractive index of the surroundings is assumed to be unity in all calculations.

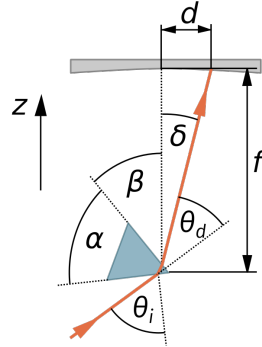


Figure A.3.: Schematic illustration of a light ray being deflected by the prism and sent to the focusing mirror in the pulse shaping setup (intermediate folding mirror omitted). Parameters relevant for calculating the lateral displacement d of a single spectral component at the focusing mirror are shown. The angles α , θ_i and θ_d are the same as in figure A.2. β describes the relative orientation of the prism and the SLM mask. δ is the the angle which the ray makes with the z -direction.

Bibliography

- [1] A. J. DeMaria, C. M. Ferrar, and G. E. Danielson. Mode locking of a nd³⁺-dopen glass laser. *Applied Physics Letters*, 8(1):22–24, 1966.
- [2] R Ell, U Morgner, FX Kartner, JG Fujimoto, EP Ippen, V Scheuer, G Angelow, T Tschudi, MJ Lederer, A Boiko, and B Luther-Davies. Generation of 5-fs pulses and octave-spanning spectra directly from a Ti:sapphire laser. *Optics Letters*, 26(6):373–375, 2001.
- [3] B Schenkel, J Biegert, U Keller, C Vozzi, M Nisoli, G Sansone, S Stagira, S De Silvestri, and O Svelto. Generation of 3.8-fs pulses from adaptive compression of a cascaded hollow fiber supercontinuum. *Optics Letters*, 28(20):1987–1989, 2003.
- [4] Matz Liebel, Christoph Schnedermann, and Philipp Kukura. Sub-10-fs pulses tunable from 480 to 980 nm from a nopa pumped by an yb:kgw source. *Optics Letters*, 39(14):4112–4115, 2014.
- [5] Hideo Ohkita and Shinzaburo Ito. Transient absorption spectroscopy of polymer-based thin-film solar cells. *Polymer*, 52(20):4397 – 4417, 2011.
- [6] AH Zewail. Femtochemistry. Past, present, and future. *Pure and Applied Chemistry*, 72(12):2219–2231, 2000.
- [7] NE Holt, D Zigmantas, L Valkunas, XP Li, KK Niyogi, and GR Fleming. Carotenoid cation formation and the regulation of photosynthetic light harvesting. *Science*, 307(5708):433–436, 2005.
- [8] SM Gallagher, AW Albrecht, TD Hybl, BL Landin, B Rajaram, and DM Jonas. Heterodyne detection of the complete electric field of femtosecond four-wave mixing signals. *Journal of the Optical Society of America B - Optical Physics*, 15(8):2338–2345, 1998.
- [9] John D. Hybl, Allison W. Albrecht, Sarah M. Gallagher Faeder, and David M. Jonas. Two-dimensional electronic spectroscopy. *Chemical Physics Letters*, 297(3–4):307 – 313, 1998.
- [10] Steven T. Cundiff and Shaul Mukamel. Optical multidimensional coherent spectroscopy. *Physics Today*, 66(7):44–49, 2013.
- [11] Minhaeng Cho. Coherent two-dimensional optical spectroscopy. *Chemical Reviews*, 108(4):1331–1418, 2008.
- [12] Jakub Dostal, Tomas Mancal, Ramunas Augulis, Frantisek Vacha, Jakub Psencik, and Donatas Zigmantas. Two-Dimensional Electronic Spectroscopy Reveals Ultrafast Energy Diffusion in Chlorosomes. *Journal of the American Chemical Society*, 134(28):11611–11617, 2012.

- [13] Jakub Dostal, Tomas Mancal, Frantisek Vacha, Jakub Psencik, and Donatas Zigmantas. Unraveling the nature of coherent beatings in chlorosomes. *Journal of Chemical Physics*, 140(11), 2014.
- [14] Steven T. Cundiff, Tianhao Zhang, Alan D. Bristow, Denis Karauskaj, and Xingcan Dai. Optical Two-Dimensional Fourier Transform Spectroscopy of Semiconductor Quantum Wells. *Accounts of Chemical Research*, 42(9):1423–1432, 2009.
- [15] Khadga J. Karki, Julia R. Widom, Joachim Seibt, Ian Moody, Mark C. Lonergan, Tonu Pullerits, and Andrew H. Marcus. Coherent two-dimensional photocurrent spectroscopy in a PbS quantum dot photocell. *Nature Communications*, 5, 2014.
- [16] T Brixner, T Mancal, IV Stiopkin, and GR Fleming. Phase-stabilized two-dimensional electronic spectroscopy. *Journal of Chemical Physics*, 121(9):4221–4236, 2004.
- [17] Patrick F. Tekavec, Geoffrey A. Lott, and Andrew H. Marcus. Fluorescence-detected two-dimensional electronic coherence spectroscopy by acousto-optic phase modulation. *Journal of Chemical Physics*, 127(21), 2007.
- [18] Saar Rahav and Shaul Mukamel. Multidimensional attosecond photoelectron spectroscopy with shaped pulses and quantum optical fields. *Physical Review A*, 81(6), 2010.
- [19] Martin Aeschlimann, Tobias Brixner, Alexander Fischer, Christian Kramer, Pascal Melchior, Walter Pfeiffer, Christian Schneider, Christian Strueber, Philip Tuchscherer, and Dmitri V. Voronine. Coherent Two-Dimensional Nanoscopy. *Science*, 333(6050):1723–1726, 2011.
- [20] Xue-Wen Chen, Ahmad Mohammadi, Amir Hossein Baradaran Ghasemi, and Mario Agio. Ultrafast coherent nanoscopy. *Molecular Physics*, 111(20):3003–3012, 2013.
- [21] Alex D Bain. Coherence levels and coherence pathways in nmr. a simple way to design phase cycling procedures. *Journal of Magnetic Resonance*, 56(3):418 – 427, 1984.
- [22] AM Weiner. Femtosecond pulse shaping using spatial light modulators. *Review of Scientific Instruments*, 71(5):1929–1960, 2000.
- [23] Antoine Monmayrant, Sebastien Weber, and Beatrice Chatel. A newcomer’s guide to ultrashort pulse shaping and characterization. *Journal of Physics B - Atomic Molecular and Optical Physics*, 43(10), 2010.
- [24] A. M. Weiner, D. E. Leaird, J. S. Patel, and J. R. Wullert. Programmable femtosecond pulse shaping by use of a multielement liquid-crystal phase modulator. *Optics Letters*, 15(6):326–328, 1990.
- [25] A.M. Weiner, D.E. Leaird, J.S. Patel, and J.R. Wullert. Programmable shaping of femtosecond optical pulses by use of 128-element liquid crystal phase modulator. *IEEE Journal of Quantum Electronics*, 28(4):908–920, 1992.
- [26] Andrew M. Weiner. *Ultrafast Optics*. Wiley Series in Pure and Applied Optics. John Wiley & Sons, Inc., 2009.

- [27] B Chatel, J Degert, S Stock, and B Girard. Competition between sequential and direct paths in a two-photon transition. *Physical Review A*, 68(4), 2003.
- [28] C Ventalon, JM Fraser, MH Vos, A Alexandrou, JL Martin, and M Joffre. Coherent vibrational climbing in carboxyhemoglobin. *Proceedings of the National Academy of Sciences of the United States of America*, 101(36):13216–13220, 2004.
- [29] D Strickland and G Mourou. Compression of amplified chirped optical pulses. *Optics Communications*, 56(3):219–221, 1985.
- [30] R. L. Fork, O. E. Martinez, and J. P. Gordon. Negative dispersion using pairs of prisms. *Optics Letters*, 9(5):150, 1984.
- [31] E. B. Treacy. Optical Pulse Compression With Diffraction Gratings. *IEEE Journal of Quantum Electronics*, 5(9):454–458, 1969.
- [32] Robert Szipöcs, Kárpát Ferencz, Christian Spielmann, and Ferenc Krausz. Chirped multilayer coatings for broadband dispersion control in femtosecond lasers. *Optics Letters*, 19(3):201–203, 1994.
- [33] F. X. Kärtner, N. Matuschek, T. Schibli, U. Keller, H. A. Haus, C. Heine, R. Morf, V. Scheuer, M. Tilsch, and T. Tschudi. Design and fabrication of double-chirped mirrors. *Optics Letters*, 22(11):831, 1997.
- [34] Thomas Binhammer, Eva Rittweger, Richard Ell, Franz X. Kärtner, and Uwe Morgner. Prism-based pulse shaper for octave spanning spectra. *IEEE Journal of Quantum Electronics*, 41(12):1552–1557, 2005.
- [35] K Yamane, T Kito, R Morita, and M Yamashita. 2.8-fs clean single transform-limited optical-pulse generation and characterization. In *Ultrafast Phenomena XIV*, pages 13–15. Optical Society of America, 2005.
- [36] Martin Aeschlimann, Michael Bauer, Daniela Bayer, Tobias Brixner, F. Javier Garcia de Abajo, Walter Pfeiffer, Martin Rohmer, Christian Spindler, and Felix Steeb. Adaptive subwavelength control of nano-optical fields. *Nature*, 446(7133):301–304, 2007.
- [37] D Goswami. Optical pulse shaping approaches to coherent control. *Physics Reports - Review Section of Physics Letters*, 374(6):385–481, 2003.
- [38] Yaron Silberberg. Quantum Coherent Control for Nonlinear Spectroscopy and Microscopy. *Annual Review of Physical Chemistry*, 60:277–292, 2009.
- [39] Meredith H. Brenner, Dawen Cai, Joel A. Swanson, and Jennifer P. Ogilvie. Two-photon imaging of multiple fluorescent proteins by phase-shaping and linear unmixing with a single broadband laser. *Optics Express*, 21(14):17256–17264, 2013.
- [40] Sang-Hee Shim and Martin T. Zanni. How to turn your pump-probe instrument into a multidimensional spectrometer: 2D IR and Vis spectroscopies via pulse shaping. *Physical Chemistry Chemical Physics*, 11(5):748–761, 2009.
- [41] A Monmayrant and B Chatel. New phase and amplitude high resolution pulse shaper. *Review of Scientific Instruments*, 75(8):2668–2671, 2004.

- [42] T Brixner and G Gerber. Femtosecond polarization pulse shaping. *Optics Letters*, 26(8):557–559, 2001.
- [43] Andrew M. Weiner. Ultrafast optical pulse shaping: A tutorial review. *Optics Communications*, 284(15, SI):3669–3692, 2011.
- [44] T. Quast. *Spectroscopic investigation of charge-transfer processes and polarisation pulse shaping in the visible spectral range*. PhD thesis, Julius-Maximilians-Universität Würzburg, 2012.
- [45] B. E. A. Saleh and M C. Teich. *Fundamentals of Photonics*. John Wiley & Sons, Inc., 2nd edition, 2007.
- [46] Jenoptik Optical Systems GmbH. *SLM-S640d Technical Documentation*.
- [47] JC Vaughan, T Feurer, KW Stone, and KA Nelson. Analysis of replica pulses in femtosecond pulse shaping with pixelated devices. *Optics Express*, 14(3):1314–1328, 2006.
- [48] M.M. Wefers and K.A. Nelson. Space-time profiles of shaped ultrafast optical waveforms. *IEEE Journal of Quantum Electronics*, 32(1):161–172, 1996.
- [49] Daan Brinks, Richard Hildner, Fernando D. Stefani, and Niek F. van Hulst. Beating spatio-temporal coupling: implications for pulse shaping and coherent control experiments. *Optics Express*, 19(27):26486–26499, 2011.
- [50] R. Baumgartner and R. Byer. Optical parametric amplification. *IEEE Journal of Quantum Electronics*, 15(6):432–444, 1979.
- [51] M. Bradler, P. Baum, and E. Riedle. Femtosecond continuum generation in bulk laser host materials with sub- μ J pump pulses. *Applied Physics B*, 97(3):561–574, 2009.
- [52] M. Bass, P. A. Franken, A. E. Hill, C. W. Peters, and G. Weinreich. Optical mixing. *Physical Review Letters*, 8:18–18, 1962.
- [53] SCHOTT AG. *Optical Glass Data Sheets*, 2015.
- [54] Flávio P. Ferreira and Michael S. Belsley. Direct calibration of a spatial light modulator by lateral shearing interferometry. *Optics Express*, 18(8):7899–7904, 2010.
- [55] Alain Bergeron, Jonny Gauvin, François Gagnon, Denis Gingras, Henri H. Arsenault, and Michel Doucet. Phase calibration and applications of a liquid-crystal spatial light modulator. *Applied Optics*, 34(23):5133–5139, 1995.
- [56] B. Döpke, J. C. Balzer, and M. R. Hofmann. In-situ calibration of spatial light modulators in femtosecond pulse shapers. *SPIE Photonics West 2014-PTO: Optoelectronic Devices and Materials*, 9004(0):90040D, 2014.
- [57] William H. Press, Saul A. Teukolsky, William T. Vetterling, and Brian P. Flannery. *Numerical Recipes in Fortran 90: The Art of Parallel Scientific Computing*. Cambridge University Press, New York, NY, USA, 2nd edition, 1996.
- [58] S. Kirkpatrick, C.D. Gelatt, and M.P. Vecchi. Optimization by simulated annealing. *Science*, 220(4598):671–680, 1983.

- [59] R Trebino, KW DeLong, DN Fittinghoff, JN Sweetser, MA Krumbugel, BA Richman, and DJ Kane. Measuring ultrashort laser pulses in the time-frequency domain using frequency-resolved optical gating. *Review of Scientific Instruments*, 68(9):3277–3295, 1997.
- [60] L. Gallmann, D. H. Sutter, N. Matuschek, G. Steinmeyer, U. Keller, C. Iaconis, and I. a. Walmsley. Characterization of sub-6-fs optical pulses with spectral phase interferometry for direct electric-field reconstruction. *Optics Letters*, 24(18):1314, 1999.
- [61] C. B. Schwarz. Erzeugung, charakterisierung und formung ultrabreitbandiger femtosekunden-laserpulse im sichtbaren spektralbereich. Master’s thesis, University of Würzburg, 2009.
- [62] Y. Yeh and C. Gu. *Optics of Liquid Crystal Displays*. John Wiley & Sons, Inc., 2009.
- [63] JA Davis, P Tsai, DM Cottrell, T Sonehara, and J Amako. Transmission variations in liquid crystal spatial light modulators caused by interference and diffraction effects. *Optical Engineering*, 38(6):1051–1057, 1999.
- [64] I. H. Malitson. Interspecimen comparison of the refractive index of fused silica*,†. *Journal of the Optical Society of America*, 55(10):1205–1209, 1965.
- [65] T. Löhrig. Planung und realisierung eines aufbaus zur formung ultrabreitbandiger fs-laserpulse im sichtbaren spektralbereich. Master’s thesis, University of Würzburg, 2007.